STRATEGIES TO INCREASE PHOTODYNAMIC THERAPY EFFICACY ON CONVENTIONAL AND COMPLEX IN VITRO CANCER MODELS

by

Mustafa Kemal Ruhi

BSc., in Physics Engineering, Hacettepe University, 2006

Submitted to the Institute of Biomedical Engineering
in partial fulfillment of the requirements
for the degree of
Doctor
of
Philosophy
in
Biomedical Engineering

Boğaziçi University
2019

ACKNOWLEDGMENTS

First, I would like to thank my parents, Serap and Fatih Ruhi, for their endless support. And to my thesis advisor, Prof. Murat Gülsoy, I offer my sincerest gratitude for his guidance.

I owe my appreciation to Assist. Prof. Ayşe Ak and Assoc. Prof. Bora Garipcan for their valuable help and contribution during my studies. I also express my thank to my other thesis committee members, Assoc. Prof. Özgür Kocatürk and Prof. İnci Çilesiz for allocating their time for critical reviewing of this thesis.

Some studies in this thesis were performed in the Wellman Center for Photomedicine, Massachusetts General Hospital. I would like to thank Prof. Tayyaba Hasan and Assist. Prof. Imran Rizvi for giving me the opportunity to work in their laboratory, to learn and explore. I would also like to thank Dr. Shubhankar Nath, Dr. Girgis Obaid and Kaitlin Moore for their guidance and support during my time in Boston.

I would like to thank Prof. Can Yücesoy, Prof. Yekta Ülgen, Assist. Prof. Hakan Solmaz and Dr. Uluç Pamuk for fostering my short but unforgettable Blues career. I would also like to acknowledge former and current members of the Biophotonics Lab and my friends at the Institute of Biomedical Engineering who made this journey fun and enjoyable.

Finally, I am grateful to Rachael Arauz and August Ventimiglia for their overwhelming hospitality during my stay in Boston.

And to my dear wife Emily, thank you for being by my side through this period, as you are through everything.

ACADEMIC ETHICS AND INTEGRITY STATEMENT

I, Mustafa Kemal Ruhi, hereby certify that I am aware of the Academic Ethics and Integrity Policy issued by the Council of Higher Education (YÖK) and I fully acknowledge all the consequences due to its violation by plagiarism or any other way.

Name :

Signature:

Date:

ABSTRACT

STRATEGIES TO INCREASE PHOTODYNAMIC THERAPY EFFICACY ON CONVENTIONAL AND COMPLEX IN VITRO CANCER MODELS

Cancer is one of the leading causes of death worldwide. Due to the side-effects and inefficacy of the conventional cancer treatment methods, alternative modalities are researched. One of the alternatives, Photodynamic Therapy (PDT), is a photochemical approach, which is based on the activation of a photosensitive chemical (photosensitizer) by a specific light source for creating reactive oxygen species that are toxic to cancer cells. A number of *in vitro* and *in vivo* studies, as well as clinical trials, are conducted every year for increasing the efficacy of PDT. Combining different photosensitizers or developing new nanoconjugations for better targeting are some of the strategies. Apart from monolayer cell cultures and *in vivo* animal models, another important tool for testing new cancer treatment strategies is an advanced *in vitro* model that mimics certain physiological factors in tumor microenvironment. These factors include cell-to-cell interactions, hypoxic environments and some mechanical stresses that may affect tumor progression. This PhD study proposes different strategies to increase photodynamic therapy efficacy and tests these new protocols on conventional and complex *in vitro* models. The outcomes of the studies not only show the success of the proposed strategies, but also reveals the importance of *in vitro* models for cancer research.

Keywords: Photodynamic Therapy, Cancer, 3D Cell Culturing, Targeting Strategies, In Vitro Models.

ÖZET

FOTODİNAMİK TERAPİ ETKİNLİĞİNİ ARTIRACAK İZLEMLERİN GELENEKSEL VE KARMAŞIK IN VITRO KANSER MODELLERİ ÜZERİNDE DENENMESİ

Kanser tüm dünyada ölüm nedenleri arasında ilk sıralarda gelmektedir. Geleneksel tedavi yöntemlerinin yan etkileri ve başarısız kaldığı durumlar nedeniyle alternatif yöntemler araştırılmaktadır. Bu alternatif yöntemlerden biri olan Fotodinamik Terapi (FDT), ışığa duyarlı bir kimyasalın (fotosensitizan) uygun bir ışık kaynağı ile uyarılması ve bu sayede ortamda kanser hücreleri için zehirli olan reaktif oksijen türlerinin oluşması prensibine dayanan fotokimyasal bir yöntemdir. PDT etkinliğini artırmak amacıyla her yıl birçok *in vitro* çalışma, hayvan deneyi ve klinik deneme yapılmaktadır. Farklı fotosensitizanları kombine etmek ve kanser hücrelerini hedeflemek için yeni nanobirleşimler geliştirmek FDT etkinliğini artırmak için araştırılmakta olan izlemlerden bazılarıdır. Klasik hücre kültürü ve hayvan modelleri dışında yeni kanser tedavi yöntemlerini denemek için kullanılan diğer bir önemli araç ise tümör mikroortamındaki bazı fizyolojik etmenleri taklit eden gelişmiş *in vitro* modellerdir. Hücre-hücre etkileşimleri, hipoksik bölgeler ve tümör gelişimini etkileyebilen mekanik uyarılar bu etmenlerden bazılarıdır. Bu doktora çalışması, fotodinamik terapi etkisini artırmak amacıyla farklı izlemler önermiş ve bu yeni protokolleri geleneksel ve karmaşık *in vitro* modeller üzerinde uygulamıştır. Sonuçlar yalnızca önerilen izlemlerin başarısını değil, *in vitro* modellerin kanser araştırmaları için önemini de ortaya koymuştur.

Anahtar Sözcükler: Fotodinamik Terapi, Kanser, 3D Hücre Kültürü, Hedefleme İzlemleri, In Vitro Modeller.

TABLE OF CONTENTS

LIST OF FIGURES

LIST OF TABLES

LIST OF SYMBOLS

ϕ	Singlet oxygen quantum yield
CO_2	Carbon dioxide
$^1O_2$	Singlet state oxygen
A	Absorption
e	Molar extinction coefficient
c	Molarity of a solution
d	Optical path length
m	Slope of a curve
F	Absorption correction factor
OD	Optical density
AI	Apoptotic index
Ap	Number of apoptotic cells
M_{ICG}	Molar weight of ICG
I_{ICG}	Number of ICG molecule
N_{A}	Avogadro number
m_{ICG}	ICG mass in one cell
J	Joule
W	Watt

LIST OF ABBREVIATIONS

PDT	Photodynamic therapy
PIT	Photoimmunotherapy
mAb	Monoclonal antibody
PIC	Photoimmunoconjugate
PC-3	Human prostate adenocarcinoma cell line
SH-SY5Y	Human neuroblastoma cell line
Caco-2	Human colorectal adenocarcinoma cancer cell line
OVCAR5	Human ovarian adenocarcinoma cell line
EPR	Enhanced permeability and retention
ROS	Reactive oxygen species
ER	Endoplasmic reticulum
ICG	Indocyanine green
DPBF	1,3-diphenylisobenzofuran
MB	Methylene blue
BPD	Benzoporphyrine derivative monoacid ring-A
EGFR	Epidermal growth factor receptor
FDA	U. S. Food an Drug Administration
ANOVA	Analysis of variance
GFR	Growth factor reduced
CI	Confidence interval
ATG5	Authophagy-related protein 5
3D	Three dimensional
2D	Two dimensional
EMT	Epithelial-mesenchymal transition

1. INTRODUCTION

1.1 Motivation

New cancer treatment methods are widely researched due to the side-effects and inefficacy of chemotherapy and radiotherapy [10, 11]. One alternative method, Photodynamic Therapy (PDT) is minimally-invasive, selective and has relatively lower side-effects than conventional cancer treatment methods [12]. Furthermore, PDT does not induce immuno-suppression and it can be combined with other cancer treatment modalities to increase the overall efficacy [13–16].

Despite its promising properties and approval in clinics, PDT is not primarily used except in the case of a few types of cancer [17]. Therefore, PDT is still a popular research field with room for development. Most studies focus on developing better photosensitizing agents or on increasing the existing photosensitizers' efficacy and selectivity. Common strategies include combining photosensitizers with one another or with different nano-constructs, such as nanoparticles, antibodies and liposomes.

The aim of this research is to test the proposed PDT enhancement strategies on different *in vitro* models. The first study investigates the potential of a promising near-infrared region photosensitizer: Indocyanine green. The second study increases PDT efficacy by combining two different formulations of BPD for targeting different organelles in cancer cells. The third study conjugates BPD with Cetuximab for selective targeting of cancer cells, which over-express epidermal growth factor receptor (EGFR). Furthermore, in the last part of the dissertation, novel *in vitro* models and their importance for cancer research are reviewed in depth.

1.2 Outline of the Thesis

Chapter 1: The thesis was introduced and the motivation of the research was presented.

Chapter 2: Background information on PDT and basic principles of PDT on cancer were indicated.

Chapter 3: The potential of indocyanine green as a PDT photosensitizer was studied on conventional cultures of three different human cancer cell lines. The study was published in Photodiagnosis and Photodynamic Therapy in January 2018 [18].

Chapter 4: Increasing the PDT efficacy by using a combination of two different formulations of the photosensitizer BPD was studied on 3D tumor spheroids. The study was published in Photochemistry and Photobiology in November 2018 [19].

Chapter 5: The review of novel *in vitro* models on cancer research was presented and a preliminary results of a EGFR-targeted PDT (PIT) study on a complex *in vitro* model was introduced.

Chapter 6: The outcomes of the thesis were revealed and the conclusions were stated.

2. BACKGROUND

2.1 Photodynamic Therapy and Photosensitizers

Photodynamic Therapy is a minimally-invasive and selective therapeutic method for treating cancer and bacterial infection [12, 20]. The procedure is based on creating cellular damage by the activation of a non-toxic photoactive chemical, photosensitizer, by using a specific light source [21].

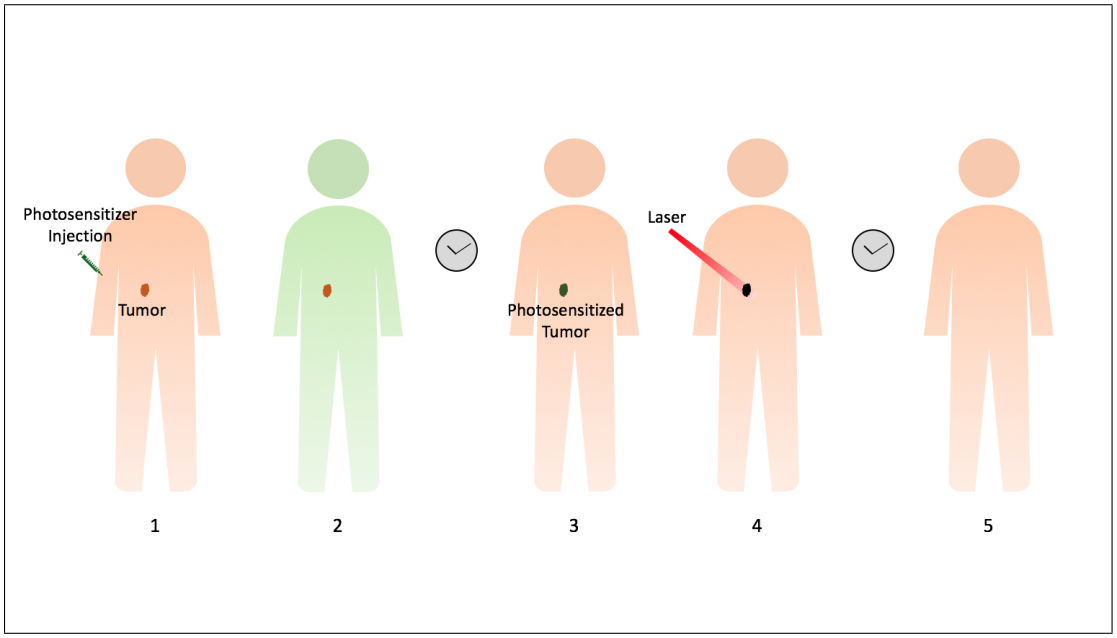

Figure 2.1 The demonstration of an anti-tumor PDT application. 1) Photosensitizer injection, 2) Spread of the photosensitizer through the body, 3) Photosensitizer is cleared from the body but accumulates in the tumor due to the enhanced permeability and retention (EPR) effect, 4) Irradiation with a specific light source, 5) Suppression of the tumor.

Once the singlet state photosensitizer absorbs the light, it becomes electronically excited. The molecule may then decay to the ground state by generating fluorescence or an intersystem crossing to the triplet energy state can take place. While returning from triplet to the ground singlet state, the molecule can react with a substrate via electron or proton transfer to form radical ions. Type I reaction occurs if these radicals react with the molecular oxygen to form Reactive Oxygen Species (ROS). A direct energy transfer from the PS molecule to molecular oxygen to form singlet oxygen is

called Type II reaction. These reactions result in an increase on the amount of singlet oxygen or other ROS, which is toxic for cancer cells or bacteria [21, 22].

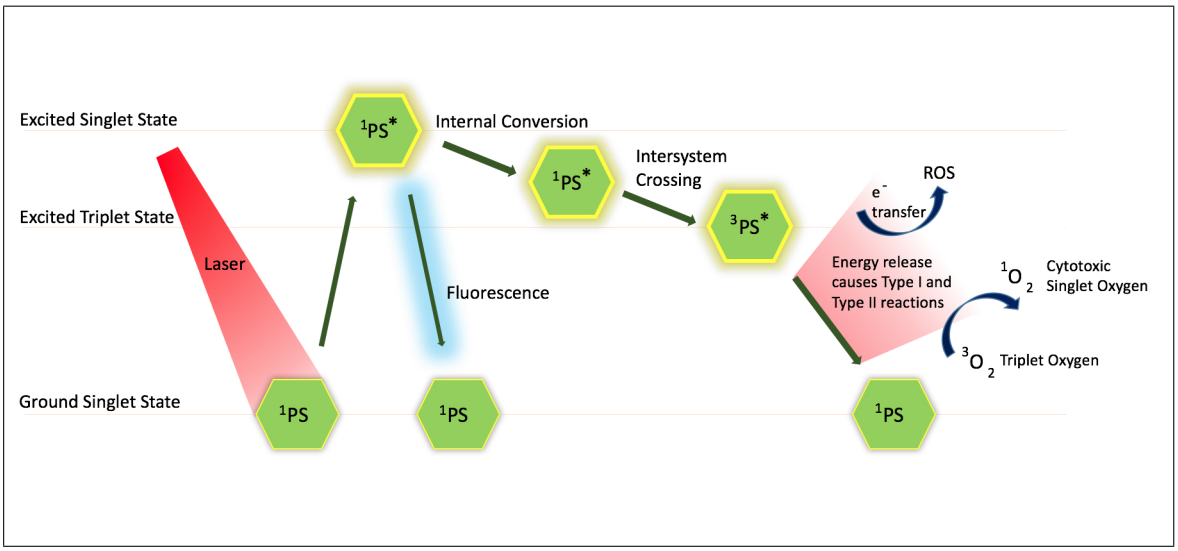

Figure 2.2 Mechanism of PDT. The singlet state photosensitizer is excited by a specific light source. Then, the photosensitizer may return to the ground state by emitting fluorescence or make an intersystem crossing to the triplet state. Type I and Type II reactions may occur while the photosensitizer molecule returns from its excited triplet state to the ground state.

The first-generation photosensitizer, "Haematoporphyrin derivative (HpD)", was used for diagnostic and therapeutic purposes; however, large doses were necessary to reach desired accumulation. Therefore, undesired photosensitivity in patients was inevitable [21]. The first clinical trial was performed in 1993 using the purified form of HpD, Photofrin, for treating bladder cancer [10, 17]. Second-generation photosensitizers, such as Benzoporphyrin, chlorin and 5-ALA were more efficient in terms of selectivity and reactive oxygen species generation [23–25]. Third-generation photosensitizers are currently being developed by using certain nano-conjugations for better delivery and targeting [24, 25].

An ideal photosensitizer should have low-dark toxicity, should be cleared rapidly from normal tissues and should have a high absorption peak at red or near-infrared region of the electromagnetic spectrum, which allows deeper penetration into tissue. Photosensitizers ideally generate a high amount of singlet oxygen and other ROS when they are activated by light. Especially in cancer treatment, where PS is injected in-

travenously, it is also important that the photosensitizer accumulates selectively in the malignant tissue [24, 26].

2.2 Photodynamic Therapy of Cancer

PDT has advantages over conventional cancer treatment modalities but it is currently used for the treatment of only a few cancer types. Damage to healthy cells or prolonged photosensitivity of patients' skin after PDT application are the drawbacks, which negatively affects the popularity of PDT. [17]. Decreasing PDT doses and increasing the selectivity of the photosensitizers are potential strategies for overcoming undesired photosensitivity in healthy tissue. The selectivity of photosensitizers can be increased by conjugating photosensitizers with different compounds [27]. For instance, a recently popular method, Photoimmunotherapy (PIT), uses monoclonal antibodies (mAb) to target certain proteins that are over-expressed on cancer cell surface, such as EGFR [28].

The effectiveness of anti-cancer PDT is strongly related to its localization within tumor tissue at the time of its activation [29]. For instance, vascular damage is considered to be the primary mechanism of tumor death if irradiation is performed while the photosensitizer molecules are in the vasculature. Otherwise, a time delay before irradiation causes the accumulation of photosensitizer in the parenchyma due to the enhanced permeability and retention (EPR) effect. In this case, a direct tumor cell destruction happens because the photosensitizer localizes either on the cell membrane or subcellular organelles and damages the concerned area [30]. Common subcellular targets in PDT are mitochondria, endoplasmic reticulum (ER) and lysosome, which are involved in energy production, protein trafficking and degradation/recycling, respectively [19]. Research has shown that photochemical damage to mitochondria leads to the release of cytochrome c, which activates apoptotic caspases. Moreover, because anti-apoptotic proteins, Bcl-2 and Bcl-xL, are found on mitochondria and ER of cancer cells, photodamage to the membrane of these organelles may affect the functionality of these proteins [27]. Similarly, the proteases that are released as a consequence of

lysosomal damage cause the cleavage of the protein Bid. The truncated Bid (t-Bid) interacts with mitochondria to release cytochrome c [31]. Lysosomes also play a crucial role in autophagy, where the cellular components are digested or recycled [32]. A third cell death mechanism, necrosis, usually occurs when the plasma membrane is damaged by PDT [27].

To conclude, increasing PDT efficacy and selectivity is important for decreasing undesired photodamage to healthy tissue and, consequently, to establish PDT in clinics. Targeting malignant cells or specific subcellular organelles in cancer cells are potential strategies for better PDT applications.

3. ANTI-CANCER PDT ON CONVENTIONAL CELL CULTURE: THE POTENTIAL OF INDOCYANINE GREEN AS A PHOTOSENSITIZER

The first study of this PhD study focuses on the near-infrared dye Indocyanine Green (ICG) to investigate its potential and weaknesses as an anti-cancer PDT agent. The following chapter is based on the article published in "Photodiagnosis and Photodynamic Therapy" in January 2018 [18].

3.1 Indocyanine green

ICG is an FDA-approved dye that is used as a contrast agent for determination of cardiac output, liver function, plasma volume, and clinical applications, such as ophthalmic angiography [33, 34]. Although it varies slightly with concentration, this particular photosensitizer is mainly excited by near-infrared light at approximately 800 nm wavelength [35, 36]. Activation by near-infrared light is advantageous for a photosensitizer because the treatment of larger tumors is possible with this wavelength range, due to the deeper tissue penetration.

The activation of ICG by near-infrared light may cause cell death by photothermal and/or photodynamic effects. There have been numerous studies supporting both arguments. For example, Mamoon *et al.* stated that with a 150 μM of ICG and 57 mW/cm^2 power density, the main effect on human melanoma cells was photodynamic [37]. Similarly, studies by Abels *et al.* and Baumler *et al.* reported singlet oxygen generation as a result of ICG-based anti-cancer studies [38,39]. Engel *et al.*, Topaloğlu *et al.* and Fickweiler *et al.* also demonstrated the photochemical effects of light-induced ICG in their research [36, 40, 41]. Conversely, there are also *in vitro* studies referring to the photothermal effects of ICG activation [42–45]. Tang *et al.* claimed that ICG can be used as a photothermal therapy agent because they observed a temperature increase over 43°C during illumination, while they kept the temperature of the culture

medium constant at 37°C [42]. Other studies supporting photothermal arguments also perceived approximately 15°C temperature increase [43–45]. The two key factors that determine an *in vitro* experiment to end up with a photothermal or photodynamic effect are the application preferences at the pre-illumination stage and the laser power density. In studies that refer to a photothermal effect, illuminations are performed without discarding the photosensitizer from the medium. This means that the excess amount of photosensitizer that was not taken up by the cells causes an extra temperature increase over the lethal level for cells. Nevertheless, the medium is always changed with phosphate-buffered saline or drug-free medium prior to illumination in experiments that report a photodynamic effect [37–41]. The laser power density is also very determinant on having different action mechanisms in an *in vitro* ICG-based experiment. Shafirstein *et al*. performed a study on murine mammary carcinoma and reported that the laser power density of 5-10 W/cm^2 with short (seconds or minutes) exposure times is convenient for photochemistry-based applications. However, short pulses of very high power densities (e.g. >100 W/cm^2) combined with intravenously administrated ICG create the photothermal effect [46].

Cellular uptake of the photosensitizer is another important parameter. The tumor accumulation of ICG has been discussed in various articles [47–50]. Onda *et al*. reported that intracellular retention of ICG in tumor cells persisted for at least 24 h, while it was rapidly cleared from normal tissue [51]. The same study showed that the distribution of ICG was cytoplasmic. Abels *et al*. similarly detected the cytoplasmic localization of ICG in skin cells by using fluorescence microscopy [38]. Some changes, such as in cytoplasmic vesiculation, chromatin condensation in the nucleus, dilation of the rough endoplasmic reticulum, the Golgi complex and the perinuclear cisternae were also observed after the activation of ICG green by diode laser. These structural findings were interpreted by the authors as proof of the photochemical effects of ICG-based therapy.

ICG-based therapy has been studied by researchers for many cancer cell lines. Tseng *et al*. reported positive results for ICG-based PDT on different pancreatic cancer cells lines [52]. Skin cancer, oral squamous cancer, breast cancer and glioblastoma

cells are some of the other cancer cell lines that have been used in similar *in vitro* studies [37, 38, 53–58]. Prostate cancer, neuroblastoma and colon cancer cell cultures, which are used in this present study, have also been studied by researchers. Prostate cancer is a commonly diagnosed disease in men, for which androgen deprivation therapy, prostatectomy and radiotherapy are known as the standard therapies [59]. Because these therapeutic modalities may lead to some side effects, such as sexual and urinary dysfunction, photodynamic therapy has been considered as a potential alternative by researchers [60,61] An ICG-based PDT study on prostate cancer cells was performed on both healthy and malignant cells by Colasanti *et al*. This *in vitro* study reported that cancer cells have stronger ICG uptake than healthy cells [15]. The authors also claimed that radiotherapy causes radio-resistance, which decreases the apoptotic cell death ratio. As a solution, the research group combined ICG-based PDT with radiotherapy, which resulted in an increase in apoptosis.

Colon cancer is another common disease that is generally observed with increasing senescence. Baumler *et al*. performed an ICG-based PDT study in 1999 on HT-29 colon cancer cells [39]. Their research focused on the effects of varying concentrations of ICG, which were previously defined by authors as non-toxic concentrations. For this purpose, 10, 50, 100 and 500 μM photosensitizer concentrations were combined with 30 J/cm^2 laser energy density, and various tests were performed. In the conclusions of the report, a significant cell viability decrease, caused mainly by singlet oxygen, was reported. Compared to the two previously studied forms of cancer, Neuroblastoma is a rare childhood disease and is mainly treated by surgical intervention, stem cell transplantation, radiation, or chemotherapy [62]. A PDT study performed on various cell lines (keratinocytes, esophagus, adenocarsinoma, colon cancer and neuroblastoma) using aminolevulinic acid (ALA-5) and methylaminolevulinate (MAL) reported that neuroblastoma was less affected by the therapy than other cell types [63]. Despite successful results, researchers also mention the drawbacks of ICG. An *in vivo* study by Abels *et al*. referred to the two weaknesses of ICG, which are short plasma half-life and low singlet oxygen quantum yield [50]. The authors indicated that high ICG concentrations should be used and only short duration treatments can be performed due to these disadvantages. The aggregation and degradation problems of

the photosensitizer in most solvents, particularly in plasma, has also been examined by researchers [34, 51, 64–66]. As mentioned by Landsman *et al.*, the relationship between absorbance and ICG concentration does not follow the Beer-Lambert law [64]. Specifically, the correlation between the absorbance and the concentration of the dye is not linear due to the aggregation. The degradation and aggregation problem directed researchers to combine ICG with various compounds. The combination of ICG with gold nanoparticles, polymeric nanoparticles or liposome to increase its effectiveness and stability is becoming a popular subject in the latest research in this field [65, 67, 68].

3.2 Aim of the study

ICG is a nontoxic, FDA-approved dye that has a strong absorption peak in the near-infrared region of electromagnetic spectrum. The properties of ICG make it a promising photosensitizer however, the dose-dependent effects and its action mechanism required further research. The aim of the present study is to investigate the potential of ICG as a PDT photosensitizer and to provide a basis for future ICG-mediated PDT studies.

3.3 Materials and methods

3.3.1 Cell lines

PC-3 (ATCC CRL-1435) human prostate adenocarcinoma cells, SH-SY5Y (ATCC CRL-226) human neuroblastoma cells and Caco-2 (ATCC HTB-3) human colorectal adenocarcinoma cells were cultured in RPMI-1640 medium nutrients (Sigma), supplemented with 10% fetal bovine serum (Sigma), 100 IU/ml penicillin, and 100 μg/ml streptomycin solution (Gibco), at 37°C in a humidified 5% CO_2 atmosphere. The culture medium was changed every three-four days and the cells were passaged when they reached confluence.

3.3.2 ICG dose determination

The cells were detached using a 0.25% (w/v) trypsin/EDTA solution, counted in a hemocytometer, and plated at a cell density of 10,000 cells per well on three 96-well polystyrene plates. The plates were incubated for 24 h to allow for cell adhesion and then the culture media were replaced with new media containing different concentrations (10, 25, 50, 75, 100, 175 and 250 μM) of ICG (Cardiogreen-Sigma). Medium was replaced with fresh medium at the end of 24 h incubation. Cell viability was assessed at the end of 24 h after ICG incubations by using MTT assay. All experiments were performed in triplicate.

3.3.3 Laser dose determination

An 808 nm wavelength computer-controlled diode laser was used in all experiments. The laser light was coupled with an optical fiber. The use of a biconvex lens allowed for the homogenous illumination of four wells at a time. The cells were detached using a 0.25% (w/v) trypsin/EDTA solution, counted in a hemocytometer and plated at a cell density of 10,000 cells per well on 96-well polystyrene plates. The plates were incubated for 24 h to allow for cell adhesion and then the culture media were renewed. After replacing the culture media with phosphate-buffered saline, the wells were illuminated in groups of four using 25, 50 and 100 J/cm^2 laser energy densities. These laser energy densities were achieved by applying 250 mW/cm^2 laser power density for 100, 200 and 400 s. Cell viability was assessed at the end of the first, second and third day by using MTT assay. All experiments were performed in triplicate.

3.3.4 Absorbance and molar extinction coefficient of ICG for aggregation investigation

The absorption spectra of ICG at 10, 25, 50, 75 and 100 μM concentrations were recorded using a Nanodrop 2000c UV-Visible spectrophotometer. The same data

was used to calculate the molar extinction coefficients based on the Beer-Lambert law (Equation 3.1).

$$A = e.c.d \tag{3.1}$$

where A = Absorption, e = The molar extinction coefficient of the solute at the wavelength of measurement, c = The molarity of the solute, d(cm) = The optical path length.

Therefore, the molar extinction coefficient "e" can be written as follows:

$$e = \frac{A}{c.d} \tag{3.2}$$

In an ideal case, the absorption of a dye solution should have a linear dependence on its concentration. Also, the molar extinction coefficient change should remain constant for each molarity and the curves of the molar extinction coefficients should overlap. If the curves of molar extinction coefficients are not similar and not overlapping in a graph, this may indicate certain concentration-dependent effects, such as aggregation [64, 69].

3.3.5 Singlet oxygen quantum yield of ICG at different concentrations

The singlet oxygen quantum yield of ICG was determined through a chemical trapping method using the fluorescent dye 1,3-diphenylisobenzofuran (DPBF). The degradation of DPBF by singlet oxygen causes a decrease on its absorption peak at 410 nm. Accordingly, if a solution that contains both DPBF and a photosensitizer is

irradiated with an appropriate light, the absorption peak of DPBF decreases proportionally to the singlet oxygen quantum yield of the photosensitizer [70–74]. The singlet oxygen quantum yield of a photosensitizer can be calculated by using a mathematical relation which compares the degradation rate of two DPBF solutions, where the second solution contains a standard photosensitizer such as Methylene blue (MB). In the present study 25, 50 and 100 μM ICG was dissolved in ethanol and subsequently mixed with a DPBF solution. The UV-Visible absorption spectrum of the sample was recorded after 15, 30 and 45 s of laser irradiation with 100 mW/cm^2 constant power density. The degradation rates of DPBF in ICG solutions were calculated from the slope of the graphs shown in Figure 3.1a, Figure 3.1b and Figure 3.1c.

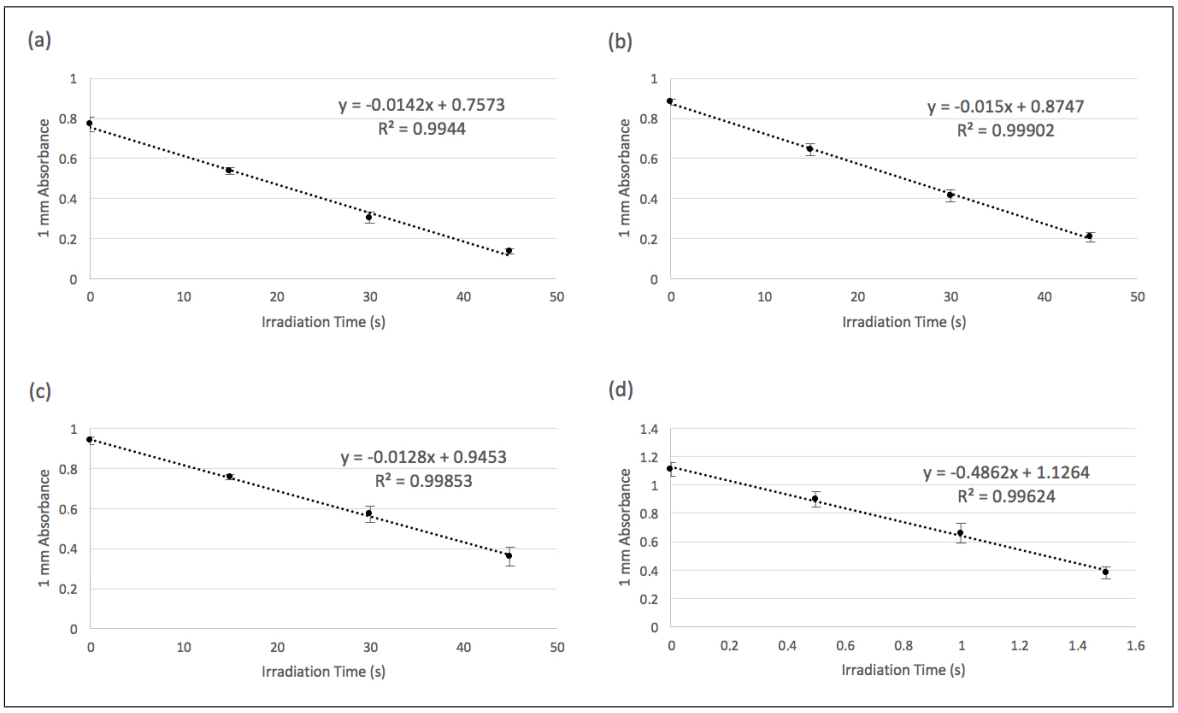

Figure 3.1 Absorbance change of DPBF at 410 nm in the presence of (a) 25 μM, (b) 50 μM, (c) 100 μM ICG and (d) 50 μM MB after constant power laser irradiation (100 mW/cm^2).

Similarly, MB at 50 μM concentration was solved together with DPBF in ethanol and irradiated for 0.5, 1 and 1.5 s with 100 mW/cm^2 laser power density. The degradation rate of DPBF in MB solution was calculated from the slope of the graph in Figure 3.1d. The singlet oxygen quantum yield of MB was taken as 0.52 [75].

The singlet oxygen quantum yields of 25, 50 and 100 μM ICG were calculated by using the following equation;

$$\phi(^1Q_2)^{\mathrm{ICG}} = \phi(^1Q_2)^{\mathrm{MB}} \frac{m^{\mathrm{ICG}}}{m^{\mathrm{MB}}} \frac{F^{\mathrm{MB}}}{F^{\mathrm{ICG}}} \tag{3.3}$$

Where ϕ is singlet oxygen quantum yield, m is the slope of DPBF absorbance change at 410 nm with constant laser power density, and F is the absorption correction factor, given by Equation 3.4.

$$F = 1 - 10^{-\mathrm{OD}} \tag{3.4}$$

(OD = Optical Density of ICG or MB at the irradiation wavelength)

3.3.6 ICG-based cancer cell inactivation experiments

Prior to the cell inactivation experiments, the cells were detached using a 0.25% (w/v) trypsin/EDTA solution, counted in a hemocytometer and plated at a cell density of 10,000 cells per well on 96-well polystyrene plates. The plates were incubated for 24 h to allow for cell adhesion and then, the culture media were replaced with new media containing different concentrations of ICG. The plates were incubated for another 24 h in order to allow for the cells to retain the photosensitizer. After replacing the culture medium with the equal amount of phosphate-buffered saline, the wells were illuminated in groups of four with different laser energy densities. These laser energy densities were achieved by applying 250 mW/cm^2 laser power for different durations. The plates were subjected to MTT assay at the end of the first, second and third day after illuminations. All experiments were performed in triplicate.

3.3.7 Temperature measurements

Previous studies state that cellular damage due to heat begins at 40°C [33, 76]. Temperature measurement during laser illumination is important in order to understand whether the mechanism of cell death is photothermal or photochemical. For this purpose, the following temperature measurements were performed using a Physitemp model MT-29/1 Type T needle thermocouple at room temperature (approximately 23°C). All temperature measurements were performed for 400 s during laser illumination with 250 mW/cm^2 laser power density because this was the highest power density used in all experiments. The following measurements were performed:

1. Temperature of the medium during experiments on three cell lines. Cells were incubated in a medium containing 100 μM ICG for 24 h prior to the experiment, which is the highest ICG dose used in all experiments. The culture media in the wells were replaced with the same volume of phosphate-buffered saline prior to light exposure in order to avoid the effect of unbounded ICG.

2. Temperature of the phosphate-buffered saline during illumination .

3. Temperature of the phosphate-buffered saline containing different concentrations of ICG (25, 50, 100 μM) during laser illumination.

All measurements were repeated at least six times.

3.3.8 Cell viability test

A colorimetric assay MTT (3-(4,5-dimethythiazol-2-yl)-2,5-diphenyl tetrazolium bromide, Glentham Life Sciences) was used to evaluate cell viability in this study. In this test, the yellow MTT is reduced to an insoluble, dark purple formazan by using mitochondrial succinate dehydrogenase. Because this reaction can only occur in viable cells, the level of the reduced MTT is a measure of cell viability. An MTT solution was

prepared, filtered, and sealed from external light sources before the experiments. 10 μl/well of MTT solution was added and the cells were incubated at 37°C for 3 h. After this incubation time, 100 μl of dimethylsulfoxide was added to each well in order to solubilize the color. Finally, the absorbance values were determined using a microplate reader because the optical absorbance values of MTT are directly proportional to viable cell numbers.

3.3.9 Apoptosis test

The highest PDT doses were applied to the cells. TUNEL (Terminal deoxynucleotidyl transferase dUTP nick end labeling) was performed using the Takara In Situ Apoptosis Detection Kit (Takara Biomedicals, Tokyo, Japan) 24, 48 and 72 h after laser illuminations. Microscope images were captured from five different positions of control and experiment wells for further counting of apoptotic and normal cells. The apoptotic index was calculated using the following formula:

$$AI = \frac{Ap}{T} \times 100 \tag{3.5}$$

where AI is the apoptotic index, Ap is the total number of apoptotic cells, and T is the total number of all cells [77, 78].

3.3.10 Reactive oxygen species detection

ROS in the cells were detected using the Enzo Total ROS Detection Kit by following the manufacturer's instructions. Briefly, the cells were cultured in 96-well plates until reaching 70% confluence. The culture medium was then replaced with a fresh medium containing 25, 50 and 100 μM of ICG. After 24 h of incubation, the oxidative stress reagent was applied to the experimental wells for 1 h. The wells

were illuminated with 250 mW/cm^2 laser power density for 100, 200 and 400 s. The fluorescence that was generated from the interaction of the ROS detection dye and reactive species was then detected under a fluorescence microscope.

3.3.11 Cellular uptake measurement

Uptake of ICG by the cells was measured as described previously by Colasanti *et al.* [15]. Briefly, 10^4 cells were seeded in a 6-well plate and incubated for 24 h to allow for cell adhesion. The culture medium of each well was then replaced with a fresh medium containing 25, 50 and 100 μM of ICG. The cells were trypsinized after another 24 h of incubation and counted using a hemocytometer. The cell suspensions were then centrifuged (1000 rpm for 5 min), the pellets were washed in phosphate-buffered saline, and the ICG was extracted by adding 500 μl of aqueous 90% acetone. Finally, the absorbance of the supernatants at 750 nm were measured using microplate reader for further calculation of ICG uptake of cancer cells. The details of this calculation is given below:

1. A standard curve was sketched by measuring the absorbance of 1-4,5 μM of ICG. (Figure 3.2)

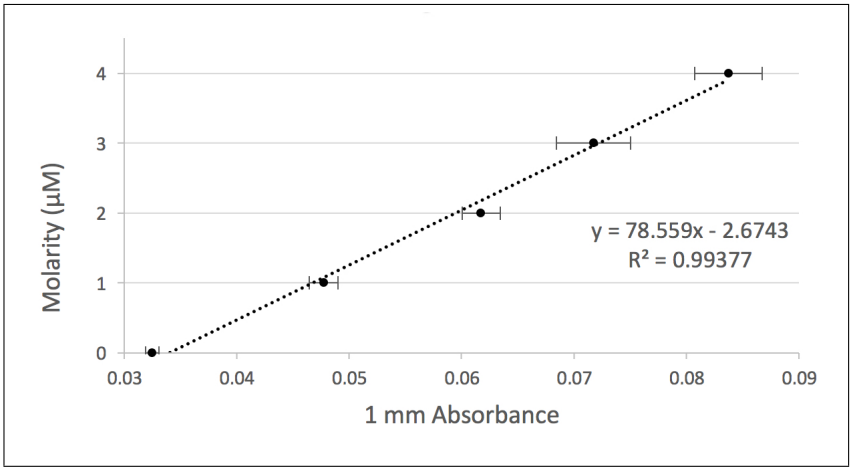

Figure 3.2 Standard curve for molarity of ICG for different absorbance values.

2. The equation for the linear relationship was determined by MS Office Excel as Equation 3.6

$$y = 78.559x - 2.674 \tag{3.6}$$

3. The molarity of each supernatant was calculated using the linear equation above. (x = average absorbance of the supernatant, y = molarity of the supernatant, R^2 = 0.994)

4. ICG quantity in one microliter of supernatant (q) was calculated as follows (M_{ICG}: Molar weight of ICG):

$$q = \frac{y(M_{\mathrm{ICG}})}{10^6} \tag{3.7}$$

5. Because the extraction solution was 500 μl, 500 times "q" gives the total ICG amount that was absorbed by the cells located in one well of the 6-well plate.

6. Division of 500q by the cell number counted from one well of the 6-well plate is equal to the approximate ICG amount that was absorbed by one individual cell.

All experiments were performed in triplicate.

3.3.12 Estimation of the singlet oxygen amount that is generated within a single cell

The cellular uptake measurements in the previous section gives the ICG mass in one cell. The number of ICG molecule in each cell was calculated using Equation 3.8;

$$I_{\mathrm{ICG}} = \frac{m_{\mathrm{ICG}}}{M_{\mathrm{ICG}}} N_{\mathrm{A}} \tag{3.8}$$

where I_{ICG} is the number of ICG molecule, m_{ICG} is ICG mass in one cell (from cellular uptake measurement data), M_{ICG} is the molar weight of ICG, and N_{A} is the Avogadro's number.

The Singlet oxygen quantum yield is the quantitative measurement of the singlet oxygen generation efficiency of a photosensitizer molecule. Therefore, the number of the singlet oxygen molecule that would be generated in each cell under identical illumination power can be calculated by multiplying the singlet oxygen quantum yield (ϕ) with the number of ICG molecule in each cell (I_{ICG}).

3.3.13 Statistical analysis

Statistical analysis was performed using the SPSS Statistics Viewer. First, the absorbance values of each group were normalized and the Shapiro-Wilk test was applied as a test for normality. Because all the data showed normal distribution, the One-Way ANOVA test was performed to determine if there is a significant difference between the groups or not. Finally, Tukey's-b test was performed to determine the groups that are statistically significantly different. The level of significance is 5% ($p \leq 0.05$) for every statistical indication in this study.

3.4 Results

3.4.1 Dose determination results

According to the first three graphs in Figure 3.3, laser energy densities of 25, 50 and 100 J/cm^2 have no inhibitory effects on the three cell lines. Moreover, Figure 3.3d reveals that 175 and 250 μM ICG concentrations cause cytotoxicity, particularly in PC-3 and SH-SY5Y cells, in more than 20% of the total cells.

Therefore, we decided to use 25, 50, 100 μM ICG concentrations and 25, 50,

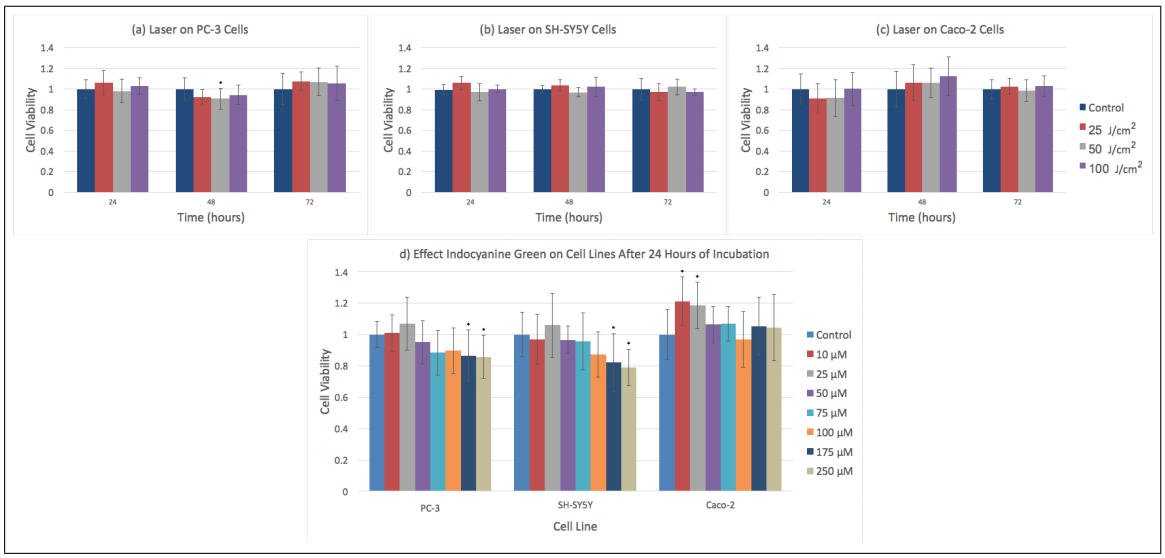

Figure 3.3 Effects of (a) 25, (b) 50 and (c) 100 J/cm^2 laser energy densities on PC-3, SH-SY5Y and Caco-2 cell viability at 24, 48 and 72$^{\text{th}}$ h. (d) Effects of different ICG concentrations on PC-3, SH-SY5Y and Caco-2 after 24 h of incubation. Groups that are statistically significantly different from the control were labeled.

100 J/cm^2 laser energy densities in the experiments.

3.4.2 UV-Visible spectroscopy of ICG for determination of aggregation behavior

In ideal solutions, there is a linear dependence between absorbance and molarity. If the molar extinction coefficient curves of different concentrations of a solute do not overlap, this is an indication of a possible aggregation based on Beer-Lambert law [64, 69]. UV-Visible absorptions of different concentrations of ICG provided the data to create the graphs in Figure 3.4.

The dissimilar curves in the Figure 3.4b are a confirmation of the aggregation problem of ICG, which was previously mentioned by Landsman *et al.* [64]

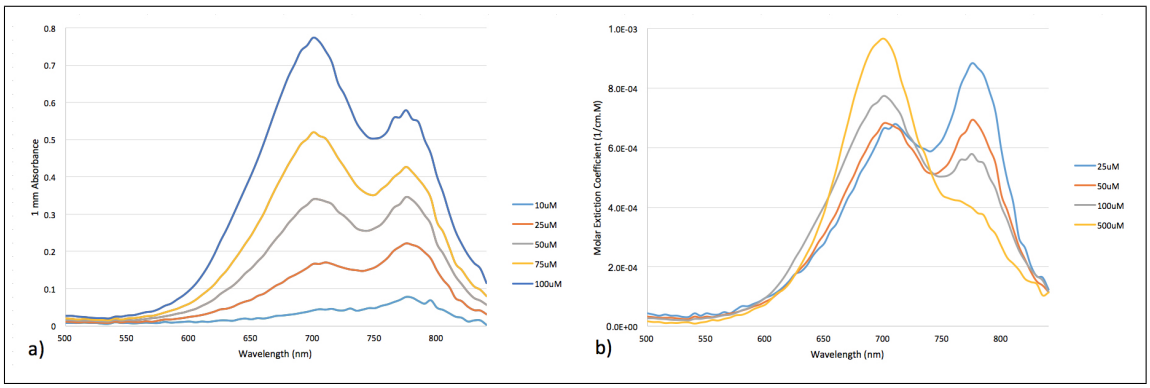

Figure 3.4 UV-Visible absorption spectrum of different ICG concentrations (a) and Molar extinction coefficient at different ICG concentrations (b).

3.4.3 Singlet oxygen quantum yield of ICG

The singlet oxygen quantum yields of 25, 50 and 100 μM of ICG were calculated as below:

$$\phi_{25} = 0.00949$$

$$\phi_{50} = 0.00684$$

$$\phi_{100} = 0.00442$$

This reveals that singlet oxygen production of ICG decreases with increasing ICG concentrations. This is likely due to the aggregation problem of ICG solutions, as mentioned in the previous section. The aggregated molecules cannot absorb the light properly and their photochemical properties change [34, 64, 69]. This causes a decrease in singlet oxygen production.

3.4.4 ICG-based cancer cell inactivation experiment results

Figure 3.5 reveals the efficacy of ICG-mediated PDT on three different cancer cell lines at the end of 24 h post-treatment incubation.

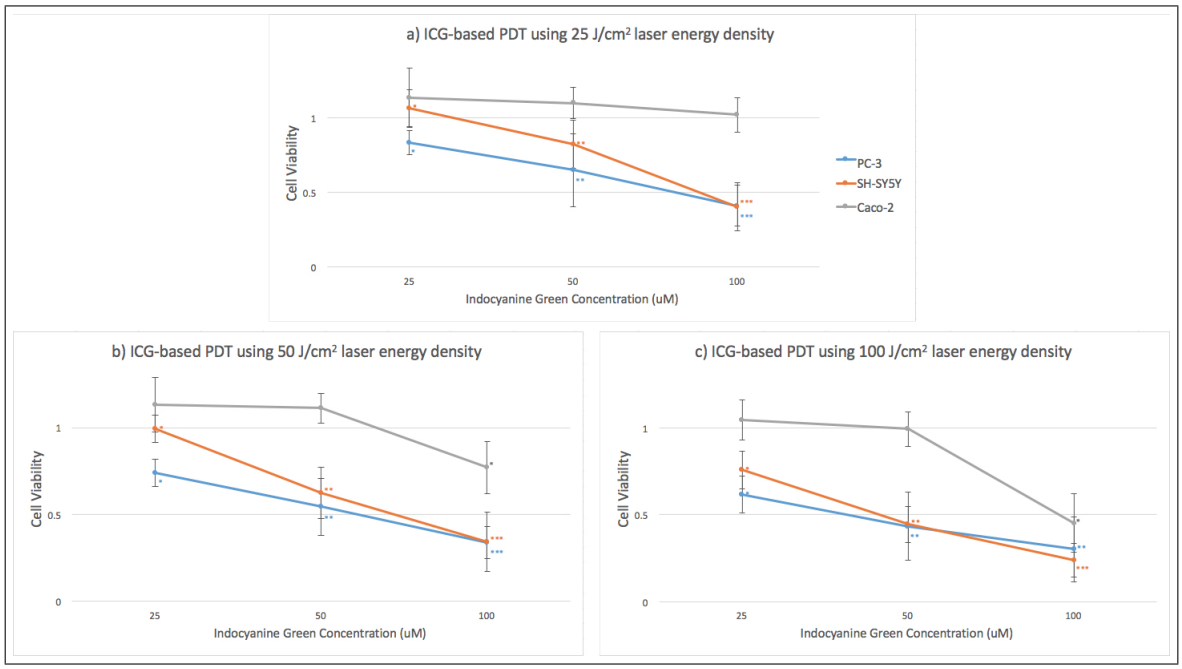

Figure 3.5 Cell viability 24 h after PDT using different ICG concentrations and (a) 25, (b) 50 and (c) 100 J/cm^2 laser energy densities.

As seen in the graphs, there is a clear decrease in cell viability with increasing ICG concentrations. It is also noticeable that colon cancer cells were less affected by the treatment. More precisely, the graphs demonstrate that 25 μM of ICG did not killed more than 50% of neuroblastoma and colon cancer cells. However, 100 μM of ICG concentration seems very efficient at every laser energy densities.

A "post-treatment incubation time"-oriented presentation of the cell viability data was presented in Figure 3.6

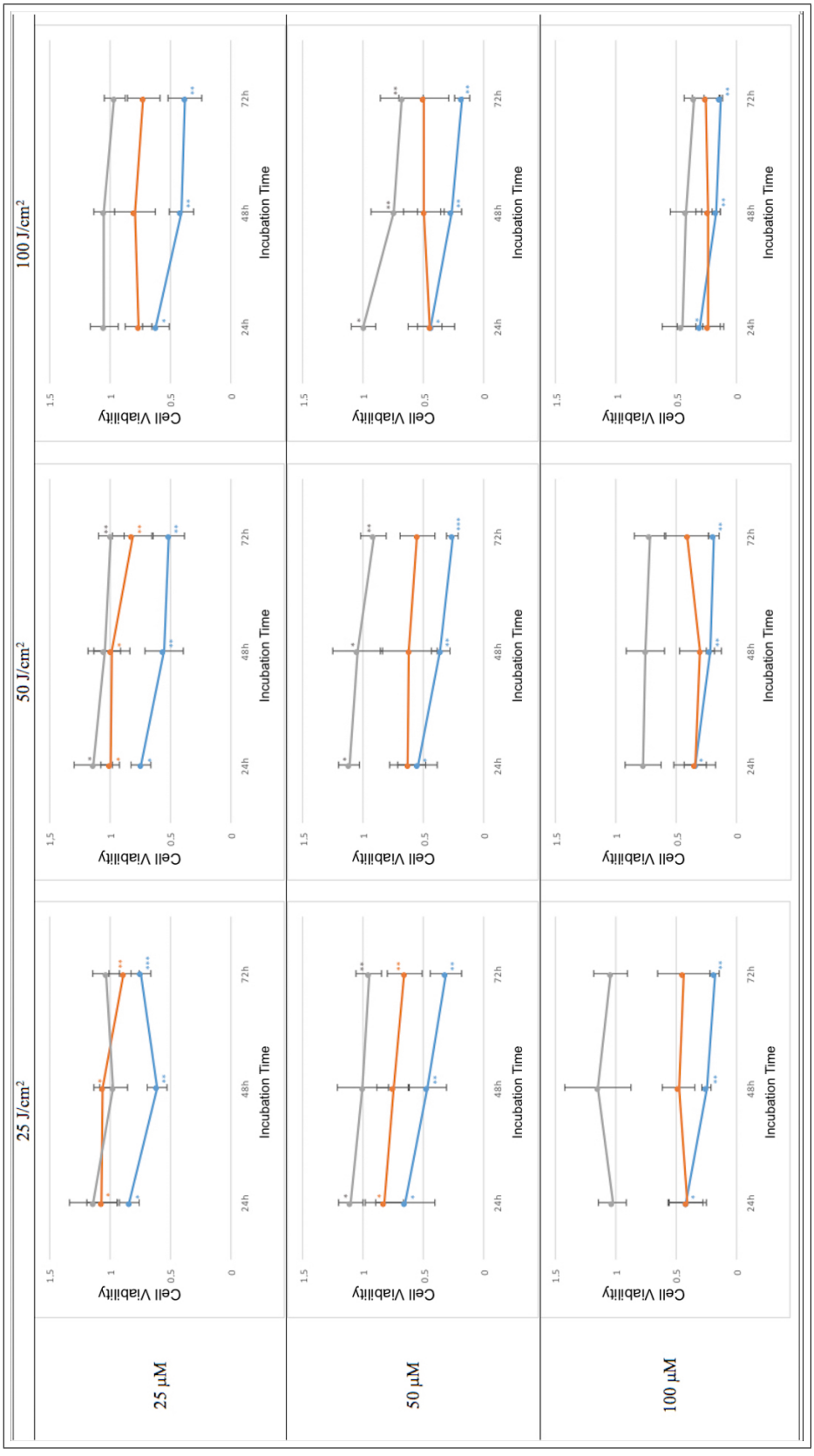

Figure 3.6 Time-oriented presentation of ICG-based cancer cell inactivation experiment results (Gray line: Caco-2, orange line: SH-SY5Y, blue line: PC-3 cells).

3.4.5 Temperature measurement results

1. The temperature of the medium did not increase more than 3°C when the ICG was discarded and fresh medium or phosphate-buffered saline was used during illumination of the cells.

2. The temperature of the phosphate-buffered saline alone did not increase more than 3°C during laser illumination.

3. In contrast, Figure 3.7 shows that there is a significant temperature increase when the ICG-containing solutions are irradiated by laser.

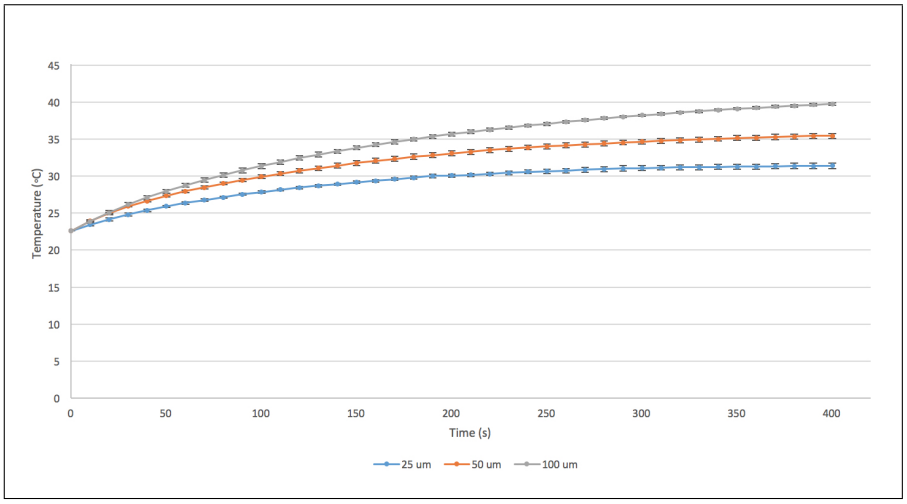

Figure 3.7 Temperature change of growth medium that contains different ICG concentrations during laser illumination (Power Density = 250 mW/cm^2).

These results reveal that a significant temperature increase may happen in *in vitro* studies, if the medium that contains ICG is not discarded before the laser illumination.

3.4.6 Apoptosis test results

Five microscope images were randomly captured from each well and, subsequently, the apoptotic and normal cells were counted (Figure 3.8).

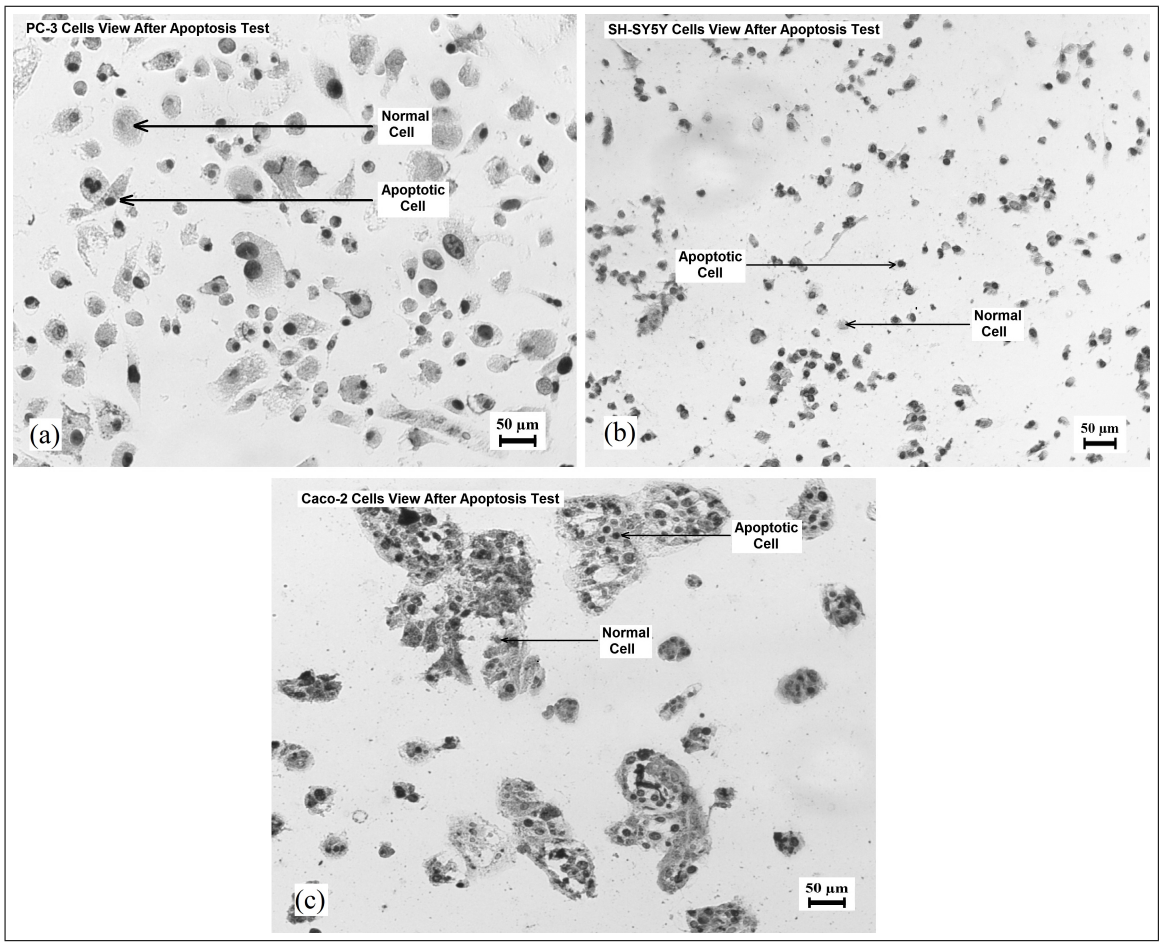

Figure 3.8 PC-3 (a), SH-SY5Y (b) and Caco-2 (c) cells after apoptosis test. Black arrows indicate some examples of the normal and apoptotic cells.

Apoptotic index averages for different incubation times are presented in Table 3.1.

Apoptosis test results indicate that all experimental groups contain 50% or more apoptotic cells. According to the Anova test results, all experimental group results are statistically significantly different from their no treatment control.

Table 3.1
Apoptotic index results.

	24 hours	48 hours	72 hours
PC-3 PDT	55.13	62.67	67.19
PC-3 Control	2.30	1.52	5.34
SH-SY5Y PDT	75.12	69.19	63.61
SH-SY5Y Control	3.79	2.33	1.08
Caco-2 PDT	56.53	68.39	49.47
Caco-2 Control	13.13	3.40	0.86

3.4.7 Reactive oxygen species detection results

The pictures taken after the oxidative stress detection reagent implementation indicate that there is a reactive oxygen species increase after the activation of ICG by near-infrared laser. Although there is a brighter cell apparition on the pictures of higher dose groups, these results were not used for the measurement of the amount of reactive oxygen species, but rather the detection thereof. Data was not shared here due to the high number of images.

3.4.8 Cellular uptake measurement results

Figure 3.9 displays the images of the centrifuge tubes before and after ICG extraction. The green color of the pellets (before) and supernatants (after) demonstrates the success of the application.

Figure 3.10 reveals that prostate cancer cells uptake more ICG than neuroblastoma and colon cancer cells. It is also clear that cellular uptake increases significantly with increasing dye concentrations.

Figure 3.9 The pictures of the centrifuge tubes before and after the successful ICG extraction.

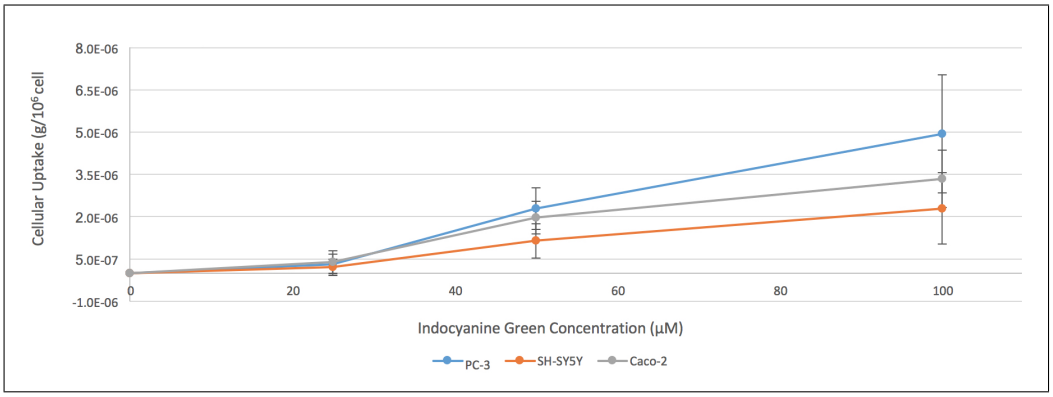

Figure 3.10 Cellular uptake of different cell lines at different ICG concentrations.

3.4.9 Singlet oxygen generation within a single cell

The number of singlet oxygen molecule that was generated in a single cell was estimated by using the calculation method explained in the Section 3.3.12.

Figure 3.11 displays the change of singlet oxygen amount in cancer cells as a result of ICG concentration increase. The increase in the singlet oxygen amount with increasing concentrations of ICG reveals that despite the poorer singlet oxygen quantum yield, 100 μM of ICG generates more singlet oxygen in the cells because it was taken up more by the cells as we observed in the previous section.

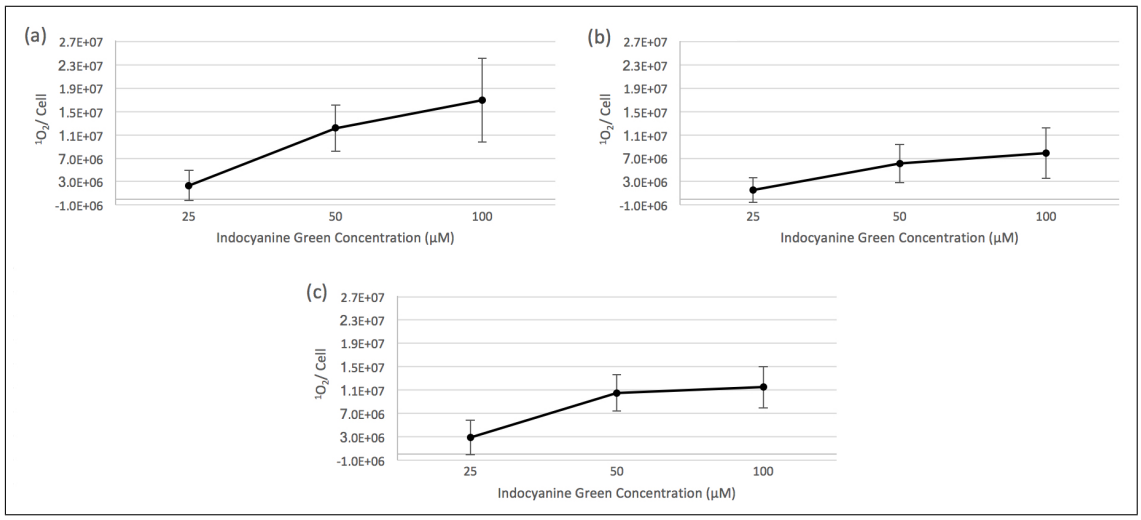

Figure 3.11 Singlet oxygen amount that is generated within in a single (a) PC-3, (b) SH-SY5Y and (c) Caco-2 cell, for different ICG concentrations.

3.5 Discussion

ICG is a nontoxic and FDA-approved dye that has a strong absorption peak in the near-infrared region of the electromagnetic spectrum. The advantageous features of ICG make it a promising photosensitizer for the photochemical or photothermal inactivation of cancer cells. However, the dose-dependent effects and its action mechanism required further research. This study addresses these points. All of the cell viability test results in this study prove the effectiveness of ICG-based therapy for three cancer cells. Furthermore, the TUNEL results demonstrate that 100 μM of ICG combined with 100 J/cm^2 laser energy density cause apoptotic death on three cancer cells. The first analysis concerning the action mechanism of this method was the singlet oxygen generation detection of ICG. The results of the experiment indicate that ICG generates singlet oxygen when it is activated by an 808 nm laser. Next, the temperature of the medium during laser illumination was monitored using a needle thermocouple. The results clearly demonstrate that the temperature of the medium did not change by more than 3°C during illumination. As mentioned previously, this result is highly dependent on the experimental procedure. If the examiner replaces the medium with phosphate-buffered saline prior to illumination, the temperature does not increase with laser exposure. However, if the laser is applied without changing the medium, the ICG

that is not absorbed by the cells causes a remarkable temperature increase. The temperature increase that we observed was very small as we expected because we used 250 mW/cm^2 laser power density and the medium was changed with phosphate-buffered saline before the illuminations. The last experiment on the action mechanism was the detection of reactive oxygen species. The images taken from the control and experimental wells show a clear fluorescence increase after laser exposure. Although the cells that were exposed to higher doses appear distinguishably brighter, this difference was not evaluated, and the findings were used for the quantification of reactive oxygen species. Taken together, these results indicate that the applied laser and ICG doses in this *in vitro* study caused cell death via photochemical effects.

Another goal of this research was to analyze the effects of dose-dependent aggregation of ICG on the cancer cell inhibition. Although previous studies have examined the aggregation problem of ICG, we presented this behavior using UV-Visible absorption spectroscopy. The singlet oxygen quantum yield of ICG at different concentrations is presented in the following section. The results show that higher concentrations of ICG generates less singlet oxygen. This is likely due to the change in photochemical and photophysical properties of aggregated ICG molecules. Aggregated molecules cannot absorb the light properly, which causes a decrease in singlet oxygen production. The characteristics of the dye can be improved by certain modifications, such as conjugations with nanoparticles or liposomes.

On the other hand, the cellular uptake results show that high concentration of ICG accumulates better in cancer cells (Figure 3.10). The question is, shall we prefer 25 μM of ICG because of its greater singlet oxygen generation or 100 μM of ICG to achieve a better cellular uptake? Figure 3.11 was sketched to answer this question by using singlet oxygen quantum yield and cellular uptake data. The graphs in Figure 3.11 indicate how singlet oxygen generation in individual cells changes with increasing ICG concentration. It is clearly seen that the singlet oxygen amount in cancer cells is higher at high ICG concentrations. The similarity between the curves in Figure 3.10 and Figure 3.11 confirm that the cellular uptake is determinant in overall singlet oxygen production. Our cell viability results are also in harmony with this prediction because

cell viability decreased with increasing ICG concentrations for each cancer cell line as seen in Figure 3.5.

Cell viability results also confirm that there is a sensitivity difference between the studied cell lines against ICG-based therapy. Cancer grade and structural dissimilarities are two of the possible reasons for the sensitivity divergence. A study by Moesta *et al.* revealed that different grades of pancreatic cancer cell lines have different photodynamic therapy results [79]. Lower degree cancer cells (also called well-differentiated cells) are more similar to normal cells and less affected by photodynamic therapy, likely because these cells have a better survival mechanisms and escape pathways. Similarly, the least-affected cells were well-differentiated Caco-2 cells, rather than poorly differentiated PC-3 and SH-SY5Y cells in our study [80–82].

Structural differences between cancer cell lines also affects their sensitivity to treatment because cell structure can influence the uptake of the photosensitizer by the cells. A study by Böhmer *et al.* reported that cell size, temperature, and pH of the medium play an important role in the uptake of haematoporphyrin derivatives by cells [83]. Cell size may be determinant specifically in terms of ICG uptake because the dye localizes in the cytoplasm. This may be interpreted as the reason for why the largest PC-3 cells absorbed the most ICG in our study (Figure 3.12)

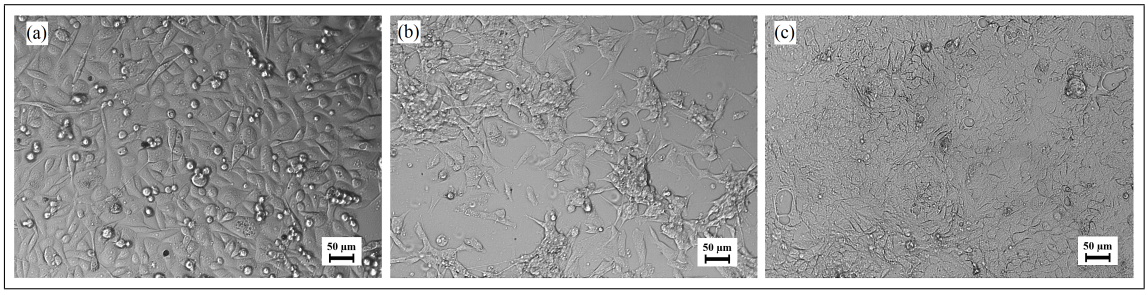

Figure 3.12 PC-3 (a), SH-SY5Y (b) and Caco-2 (c) cells. Scalebar: 50 μm.

Another reason for the uptake difference between the cell lines can be the tight junction formations of neighboring cells. As Onda *et al.* discussed, tight junction formation is a factor that decreases the ICG uptake of cells. This can be studied through various staining methods [51].

In conclusion, we demonstrated that ICG can be used as an efficient photochemical agent in cancer treatment. However, the overall results are not conclusive enough for clinical use of ICG due to the low singlet oxygen yield and aggregation problems. Follow-up studies were designed and are currently being conducted in our laboratory. Therefore, apart from providing insight into ICG-mediated PDT, this research also constituted a basis for studies that are aiming to improve ICG properties and to overcome resistivity to PDT.

4. A STEP BEYOND CONVENTIONAL MODELS AND CLASSICAL PDT: ENHANCED PDT BY A COMBINATION STRATEGY ON 3D TUMOR MODEL

The second study of the thesis was conducted in Wellman Center for Photomedicine - Massachushets General Hospital under the supervision of Prof. Tayyaba Hasan and Assist. Prof. Imran Rizvi. The following chapter is based on the article published in the 55th Commemorative Issue of "Photochemistry and Photobiology" in November 2018 [19]. Contributors to this study included Assist. Prof. Imran Rizvi, Dr. Shubhankar Nath, Dr. Girgis Obaid, Kaitlin Moore, Dr. Shazia Bano, Prof. Tayyaba Hasan and Prof. David Kessel.

4.1 BPD and Visudyne

Benzoporphyrin derivative monoacid ring-A (BPD) is a second generation photosensitizer that has a respectively high singlet oxygen quantum yield [84]. BPD accumulates rapidly in tumor and it is toxic to cancer cells [85]. Furthermore, BPD can be activated by 690 nm light, which is a preferable wavelength in terms of penetration to tissue.

Visudyne is the FDA-approved non-pegylated nanoliposomal for of BPD for intravenous injection [86]. Research has revealed that BPD binds to mitochondria and ER inside cancer cells [87, 88].

4.2 Aim of the study

Different photosensitizers localize on different organelles in a cancer cell. Depending on the PS localization, various cellular and subcellular components can be targeted, causing selective photodamage [17]. It has been shown that targeted lyso-

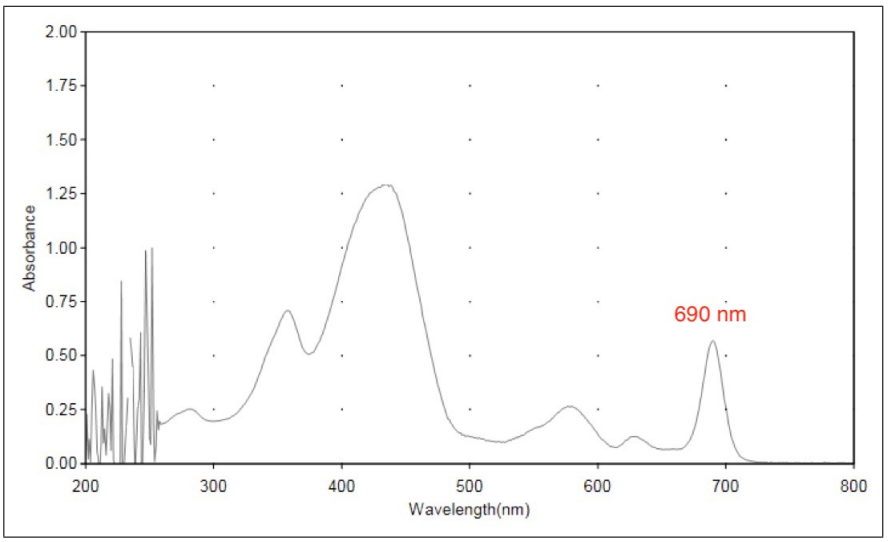

Figure 4.1 UV-Visible absorption spectrum of Visudyne. An absorption peak exists at 690 nm wavelength.

somal photodamage followed by, or simultaneous with, mitochondrial photodamage using two different photosensitizer results in a considerable enhancement in PDT efficacy [89–91].

The aim of this study is to increase PDT efficacy by targeting different organelles in cancer cells such as lysosome, mitochondria and ER. The two different liposomal formulations of BPD were used in the experiments to simultaneously target lysosome and mitochondria/ER by a single laser irradiation. The experiments were conducted on both conventional cell cultures and on 3D tumor spheroids.

4.3 Materials and methods

4.3.1 Cell line

Human ovarian carcinoma cells NIH:OVCAR5 (OVCAR5) were acquired from Fox Chase Cancer Center (Philadelphia, PA, USA). Cells were maintained in T75 flask at 37°C incubator with RPMI 1640 medium (Mediatech Inc., Herndon, Virginia, USA) containing 10% (v/v) heat inactivated FBS (GIBCO Life Technologies, Grand

Island, New York, USA) and 1% Penicilin/Streptomycin. OVCAR5-mCherry cells were generated previously, via transducing OVCAR5 cells with lentiviruses encoding an mCherry gene by Dr. Shubhankar Nath [19].

4.3.2 3D cell culturing

3D OVCAR5-mCherry spheroids were grown and maintained for 11 days on Growth Factor Reduced (GFR) Matrigel (Corning 354230, lot # 7016289) beds. GFR Matrigel was thawed overnight on ice. Matrigel beds were prepared by plating 250 μL of Matrigel solution on pre-chilled 24-well black-wall plate (Krystal 24 Well Microplate or Greiner Bio-One 24-well glass bottom Sensoplate). Matrigel beds were polymerized by incubating at 37°C for 20-25 minutes. OVCAR5-mCherry cells grown in monolayer were washed with PBS and trypsinized. Cells were counted and plated at a density of 10,000 cells/well in 1 mL of 2% GFR Matrigel-containing complete growth medium. 3D cultures were maintained at 37°C in an atmosphere of 5% CO_2. The growth media was replaced every 3 and 6/7 days.

4.3.3 Two liposomal formulations of BPD

Visudyne, non-pegylated nanoliposomal form of BPD, was purchased from Bausch + Lomb. BPD was purchased from U.S. Pharmacopeia. Cholestrol-free 16:0 lyso PC-BPD (lipid-anchored BPD) liposomes were prepared previously by the members of the Hasan Laboratory. Briefly, 16:0 lyso PC-BPD was first prepared and purified. Then, the lipid-anchored BPD liposomes were prepared by the thin film hydration technique under dark conditions and were designed to be moderately cationic to promote cellular uptake [19, 88].

The BPD equivalent concentration in the lipid-anchored BPD liposomes and Visudyne was quantified using absorption spectrophotometry ($\varepsilon_{687\text{nm}}$ = 34,895 $M^{-1}.cm^{-1}$).

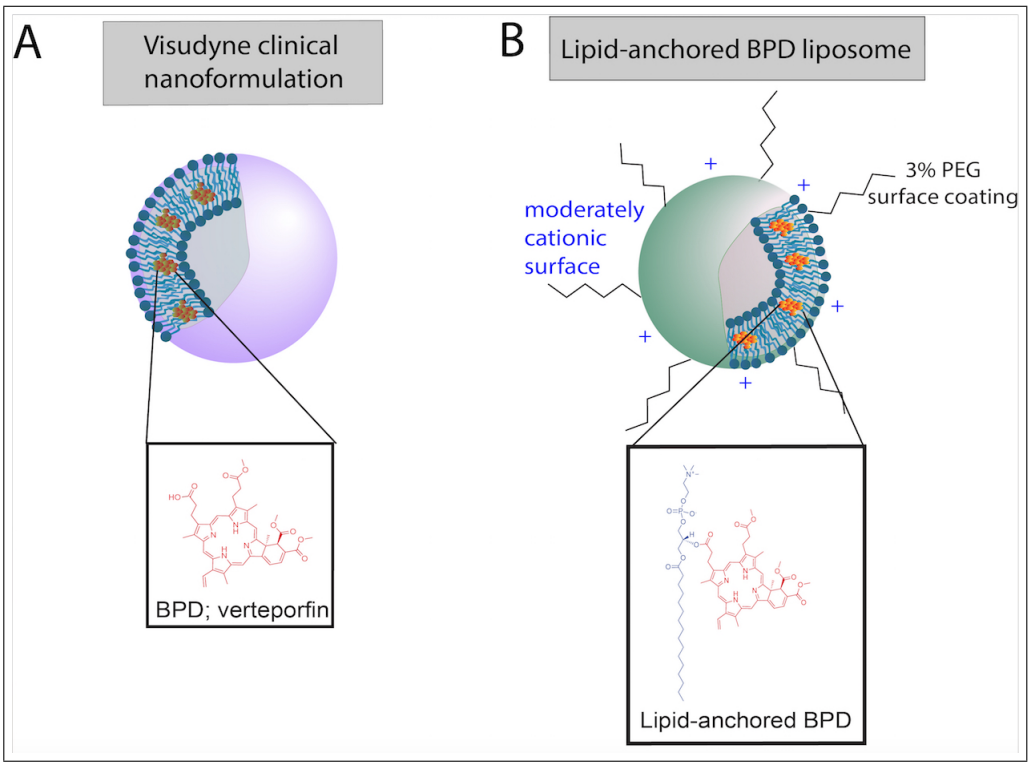

Figure 4.2 (a) Structure of Visudyne. BPD is associated with the lipid bilayer of the liposome. (b) The lipid-anchored BPD liposome formulation has a moderately cationic surface and is coated with 3% PEG. BPD is conjugated to a lipid in the bilayer of the liposome.

4.3.4 Evaluation of treatment response

Cell viability of monolayer wild-type OVCAR5 cells was assessed with MTT assay. The yellow MTT is reduced to an insoluble, dark purple formazan by using mitochondrial succinate dehydrogenase in viable cells. The level of the reduced MTT is a measure of cell viability. An MTT solution was prepared, filtered, and sealed from external light sources before the experiments. 10 μl/well of MTT solution was added and the cells were incubated at 37°C for 3 h. After this incubation time, 100 μl of dimethylsulfoxide was added to each well in order to solubilize the color. Finally, the absorbance values were determined using a microplate reader because the optical absorbance values of MTT are directly proportional to viable cell numbers.

Cell viability of 3D cultures was evaluated by measuring mCherry fluorescence that is emitted from live cells, using Operetta CLS High Content Image Analysis System (Perkin Elmer). First, the excitation and emission spectrums of BPD and mCherry

were compared to make sure that there were no undesired cross-excitations. Then, mCherry fluorescence was detected using an excitation LED of 530-560 nm and an emission filter of 570-650 nm. Images were acquired using 5X air objective lens (N.A. of 0.16) in multiple z-stacks (between 10-14) with 50 μm step size. During imaging, the chamber of the system was kept at 37°C with 5% CO_2. Acquired images were analyzed using Harmony 4.6 software (Perkin Elmer). In brief, image mosaics were joined together for each plane and every z-plane images were combined to construct a final 2-dimensional image for each well. A threshold for mCherry fluorescence was determined at the beginning of each analysis based on the "No Treatment Control" to establish the "Live Tumor Area".

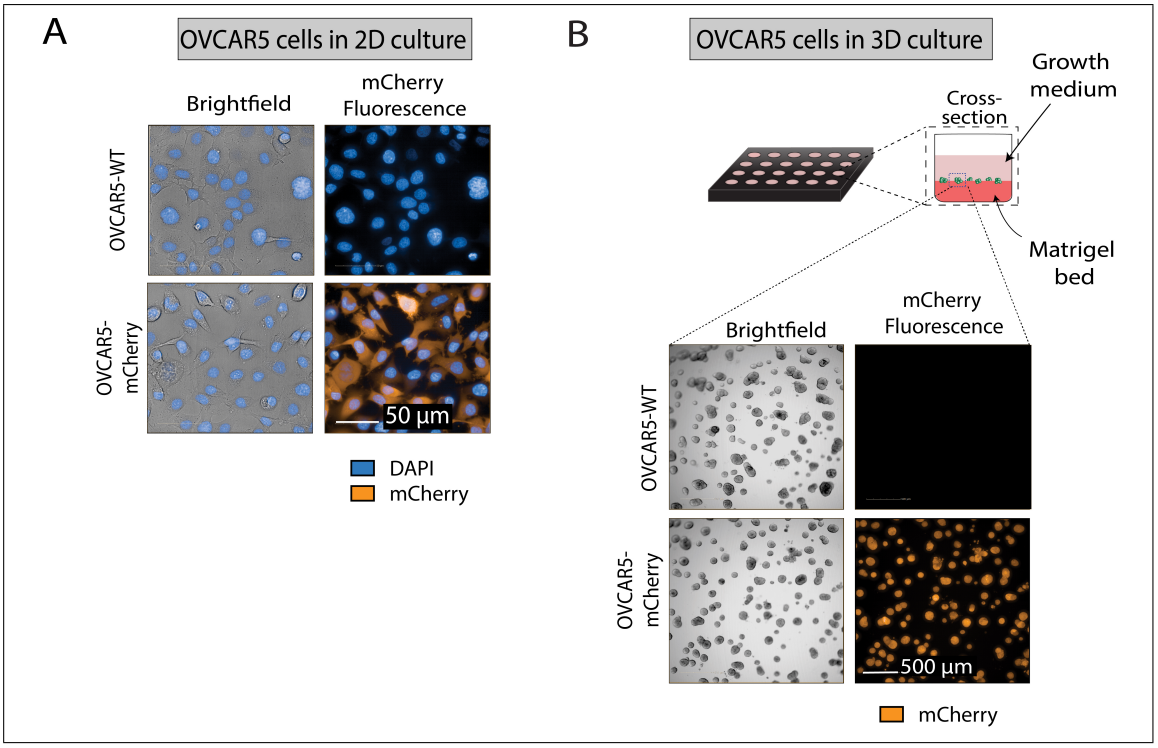

Figure 4.3 (a) Wild-type OVCAR5 and OVCAR5-mCherry cells grown in conventional 2D monolayer. Cells were stained with DAPI (blue) and imaged for brightfield (grey) and mCherry (orange) fluorescence. (b) In the 3D culture model, OVCAR5 cells form spheroids on a Matrigel bed in the wells of a 24-well plate.

4.3.5 Statistics

One-way analysis of variance (ANOVA) was followed by Dunnett's multiple comparison test using GraphPad Prism 7. Statistically significantly different groups were

labeled corresponding to the p values. Treatment groups were internally normalized to respective no treatment controls, and results are reported as median ±95% confidence interval (CI). All graphs represent data acquired from at least 3 independent experiments in triplicate for each group.

4.3.6 Visudyne-mediated PDT on conventional monolayer cell cultures

Visudyne-mediated PDT was first applied on conventional 2D cell cultures of wild-type OVCAR5 and OVCAR5-mCherry. The cells were incubated with Visudyne (BPD equivalent concentration of 1.0 μM) for 90 minutes. The cell viability was assessed using MTT assay, 24 hours after the irradiation with 690 nm at different laser energy densities (Irradiance: 50 mW/cm^2). The experiment timeline is presented in Figure 4.4

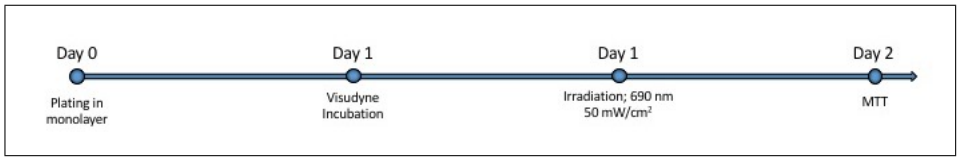

Figure 4.4 Experiment timeline for Visudyne-mediated PDT on monolayer cell cultures.

4.3.7 Visudyne-mediated PDT on 3D tumor spheroids

OVCAR5 cells were plated on Matrigel on day 0 in 1 ml of 2% GFR-Matrigel in RPMI complete growth medium. 3D cell cultures were incubated with Visudyne (BPD equivalent concentration of 1.0 μM) for 90 minutes on day 7. The cell viability was assessed using mCherry fluorescence, 4 days after the irradiation with 690 nm at different laser energy densities (Irradiance: 50 mW/cm^2). The experiment timeline is presented in Figure 4.5

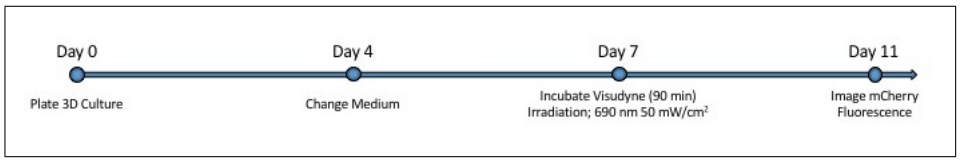

Figure 4.5 Experiment timeline for Visudyne-mediated PDT on 3D tumor spheroids.

4.3.8 Lipid-anchored BPD liposome-mediated PDT on 3D tumor spheroids

Following the 3D plating of OVCAR5-mCherry cells on day 0, 3D cell cultures were incubated with Lipid-anchored BPD liposome (BPD equivalent concentration of 1.0 μM) for 24 hours on day 6. The cell viability was assessed 4 days after irradiation with 690 nm laser for increasing time periods (Irradiance: 50 mW/cm^2). The experiment timeline is presented in Figure 4.6

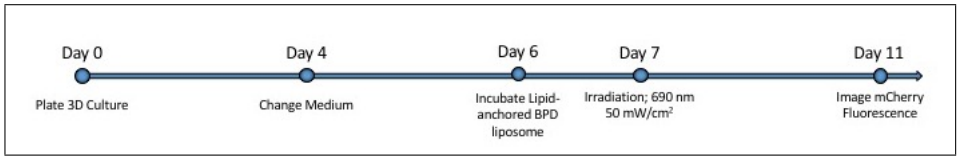

Figure 4.6 Experiment timeline for lipid-anchored BPD-mediated PDT on 3D tumor spheroids.

4.3.9 Enhanced PDT by using the combination of two liposomal formulations of BPD on 3D tumor spheroids

3D cultures of OVCAR5-mCherry cells were first incubated with Lipid-anchored BPD liposome (BPD equivalent concentration of 1.0 μM) for 24 hours. Then, the culture media were changed with Visudyne containing (BPD equivalent concentration of 1.0 μM) complete RPMI. Irradiation was performed at the end of 90 minutes of incubation with Visudyne. The cell viability was assessed 4 days after irradiation with 690 nm laser for increasing time periods (Irradiance: 50 mW/cm^2). The experiment timeline is presented in Figure 4.7

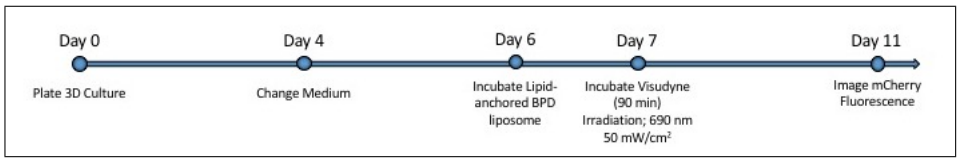

Figure 4.7 Experiment timeline for lipid-anchored BPD liposome and Visudyne combination PDT on 3D tumor spheroids.

4.4 Results

4.4.1 Results of Visudyne-mediated PDT on conventional cell cultures of wild-type OVCAR5 and OVCAR5-mCherry cells

Visudyne-mediated PDT is an effective treatment method on both wild-type and mCherry expressing OVCAR5 cells. The cell viability of both cells in monolayer decreases with increasing laser energy densities. Laser energy density groups are statistically significantly different from each other but there is no significant difference between the response of mCherry and wild-type OVCAR5 cells to the treatment. All data were internally normalized to respective no treatment controls, as indicated by the dashed line.

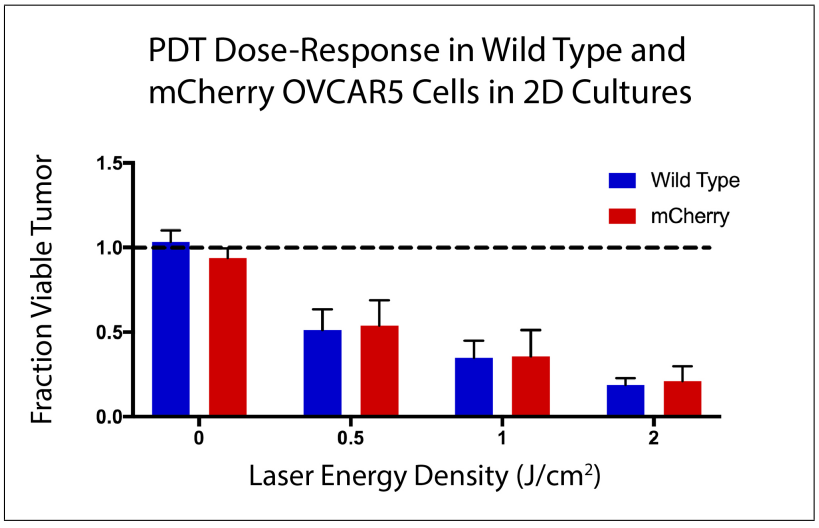

Figure 4.8 The results of Visudyne-mediated PDT on monolayer wild-type OVCAR5 and OVCAR5-mCherry cell cultures.

4.4.2 Results of Visudyne-mediated PDT on 3D tumor spheroids

To evaluate the efficacy of Visudyne PDT alone, 3D cultures were incubated with 1.0 μM BPD equivalent for 90 minutes, on day 7 post-plating. Following the incubation period, the medium was aspirated and replaced with fresh culture medium. The tumors were irradiated with energy densities ranging from 0.5 to 10 J/cm^2 at an irradiance of 50 mW/cm^2. The results reveal that the same concentration of Visudyne is less effective on 3D cell culture, than it was on 2D cell culture, as expected. 3D tumor spheroids are more resistant to therapies because the cells at the inner region of the spheroids are less affected from the treatment due to the hypoxia and screening by outer layers of cells. The results were presented as box and whisker plots to provide a better insight of the data.

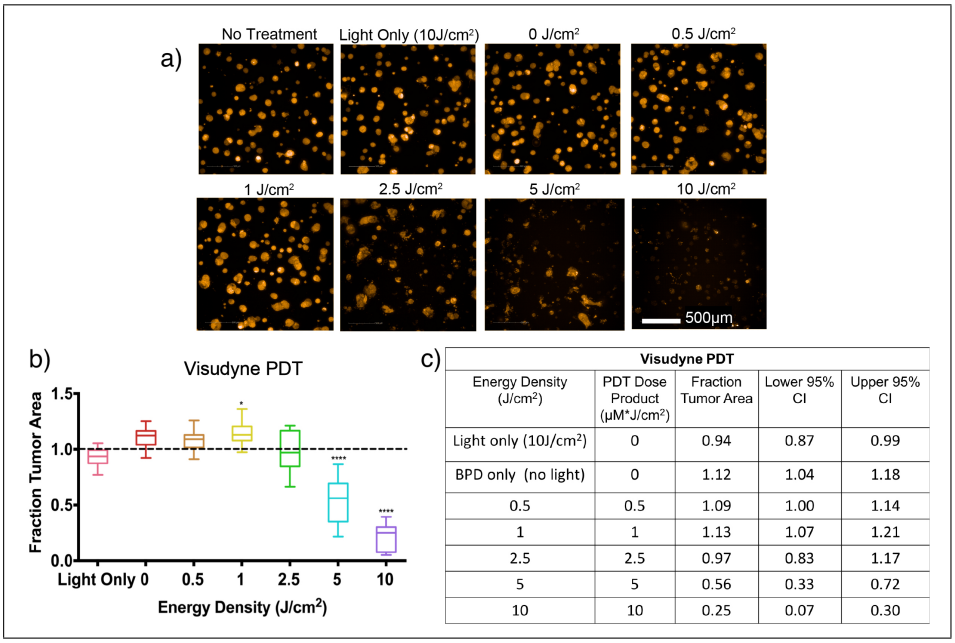

Visudyne PDT				
Energy Density (J/cm²)	PDT Dose Product (µM*J/cm²)	Fraction Tumor Area	Lower 95% CI	Upper 95% CI
Light only (10J/cm²)	0	0.94	0.87	0.99
BPD only (no light)	0	1.12	1.04	1.18
0.5	0.5	1.09	1.00	1.14
1	1	1.13	1.07	1.21
2.5	2.5	0.97	0.83	1.17
5	5	0.56	0.33	0.72
10	10	0.25	0.07	0.30

Figure 4.9 (a) Decreasing mCherry fluorescence with increasing PDT dose (scalebar: 500 μm) and the corresponding dose-response plot in (b). All data were internally normalized to respective no treatment controls, as indicated by the dashed line. Groups that are statistically significant from no treatment are labeled (*: p$<$ 0.05, ***: p$<$ 0.001, ****: p$<$ 0.0001). All values are reported as median $\pm$95% CI. The table in (c) summarizes energy density (in J/cm^2), PDT dose product, median fraction of tumor area remaining after treatment, and upper and lower 95% confidence intervals of the median. The PDT dose product is the energy density (in J/cm^2) multiplied by the concentration of PS administered (μM) (in this case 1μM). All groups, except no treatment and light only, received Visudyne (1.0 μM BPD-equivalent).

4.4.3 Results of Lipid-anchored BPD liposome-mediated PDT on 3D tumor spheroids

A similar protocol was followed to determine PDT efficacy using the lipid-anchored BPD liposome in 3D cultures. Based on previously published data [88], a longer incubation period (24 hours) and substantially higher energy densities (10 - 60 J/cm^2 at 50 mW/cm^2) were used for these experiments. As shown in the panel of representative mCherry fluorescence images (Figure 4.10a) and the corresponding plot (Figure 4.10b), PDT with lipid-anchored BPD liposomes resulted in no significant reduction in fraction tumor area at energy densities ranging from 0 J/cm^2 (lipid-anchored BPD liposomes alone) to 40 J/cm^2. A significant but modest reduction in fraction tumor area was seen at an energy density of 50 J/cm^2 (0.82, CI = 0.86, 0.64, p<0.001). A 20% increase in the light dose (to 60 J/cm^2) produced only a small improvement in efficacy (median fraction tumor area 0.74, CI = 0.82, 0.55, p<0.0001).

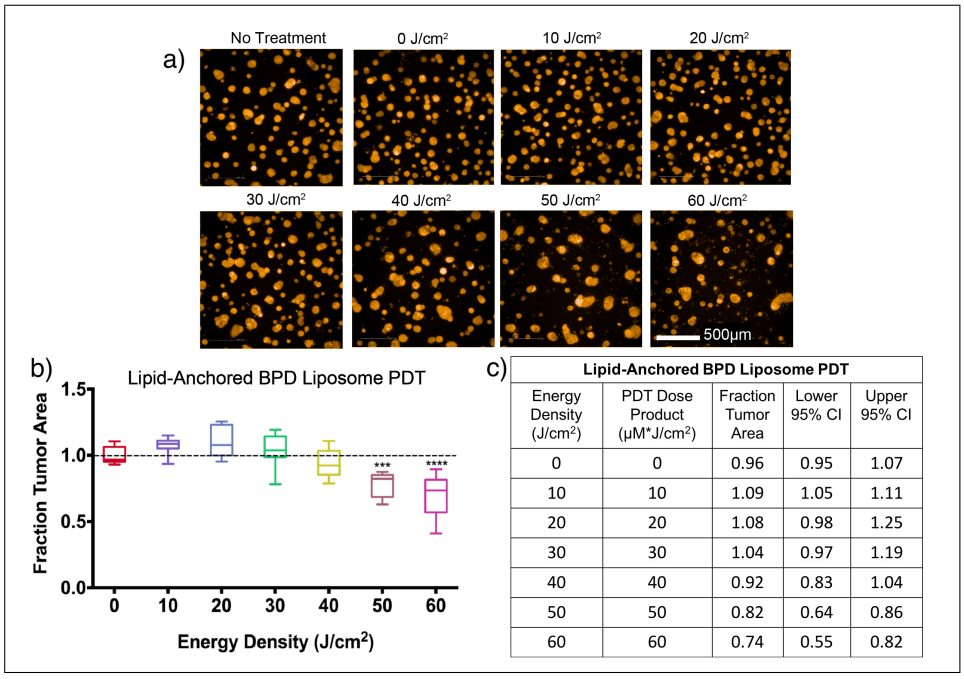

Lipid-Anchored BPD Liposome PDT				
Energy Density (J/cm^2)	PDT Dose Product (µM*J/cm^2)	Fraction Tumor Area	Lower 95% CI	Upper 95% CI
0	0	0.96	0.95	1.07
10	10	1.09	1.05	1.11
20	20	1.08	0.98	1.25
30	30	1.04	0.97	1.19
40	40	0.92	0.83	1.04
50	50	0.82	0.64	0.86
60	60	0.74	0.55	0.82

Figure 4.10 (a) Decreasing mCherry fluorescence with increasing PDT dose (scalebar: 500 μm) and the corresponding dose-response plot in (b). All data were internally normalized to respective no treatment controls, as indicated by the dashed line. Groups that are statistically significant from no treatment are labeled (***: p< 0.001, ****: p< 0.0001). All values are reported as median ±95% CI. The table in (c) summarizes energy density (in J/cm^2), PDT dose product, median fraction of tumor area remaining after treatment, and upper and lower 95% confidence intervals of the median. All groups, except no treatment and light only, received Lipid-anchored BPD liposome (1.0 μM BPD-equivalent).

4.4.4 Results of PDT by using the combination of two liposomal formulations of BPD on 3D tumor spheroids

PDT with combination of Visudyne and lipid-anchored BPD liposome significantly enhances efficacy relative to individual therapies in a 3D tumor model. In the experiments, where Visudyne or lipid-anchored BPD liposome were used alone as photosensitizers, no significant reduction in fraction tumor area was observed at 2.5 J/cm^2, For the combination experiments, this laser energy density caused around 90% decrease in the fraction tumor area (Figure 4.11). The PDT dose product should also be considered while evaluating the results. A PDT dose product of 5 μM . J/cm^2 (2 μM BPD equivalent administered times 2.5 J/cm^2) with the combination protocol reduced median fraction tumor area to 0.09 (CI = 0.23, 0.05, p<0.0001). A comparable dose product with Visudyne PDT (1 μM BPD equivalent administered x 5 J/cm^2) (Figure 4.9c) resulted in a median fraction tumor area of 0.56 (CI = 0.72, 0.33, p<0.0001).

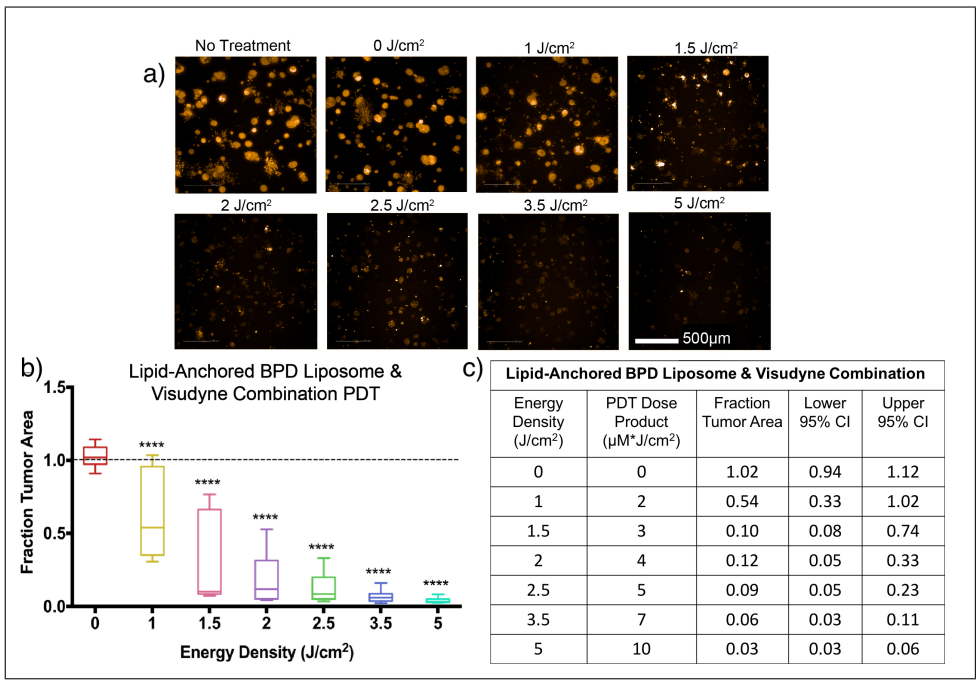

Energy Density (J/cm^2)	PDT Dose Product (µM*J/cm^2)	Fraction Tumor Area	Lower 95% CI	Upper 95% CI
0	0	1.02	0.94	1.12
1	2	0.54	0.33	1.02
1.5	3	0.10	0.08	0.74
2	4	0.12	0.05	0.33
2.5	5	0.09	0.05	0.23
3.5	7	0.06	0.03	0.11
5	10	0.03	0.03	0.06

Figure 4.11 (a) Decreasing mCherry fluorescence with increasing PDT dose (scalebar: 500 μm) and the corresponding dose-response plot in (b). All data were internally normalized to respective no treatment controls, as indicated by the dashed line. Groups that are statistically significant from no treatment are labeled (****: p< 0.0001). All values are reported as median ±95% CI. The table in (c) summarizes energy density (in J/cm^2), PDT dose product, median fraction of tumor area remaining after treatment, and upper and lower 95% confidence intervals of the median.

4.5 Discussion

The selectivity of PDT depends on factors, such as spatial confinement of light and the localization of photosensitizer [16, 92, 93]. In the context of therapies for cancer, rational targeting of multiple tumor compartments or sub-cellular sites have been shown to enhance photodynamic efficacy [32, 85, 88–91, 94–98].

The FDA-approved liposomal formulation of BPD, Visudyne, preferentially localizes on mitochondria and ER [16,92]. Therefore, the activation of Visudyne by light causes photodynamic disruption of the mitochondrial membrane, which triggers the release of cytochrome c, a potent initiator of cell death [93, 99–101]. Recent studies have shown that prior or simultaneous photodamage to lysosomes using NPe6 significantly increases the effect of mitochondrial-targeted PDT [32, 89, 91]. Possible mechanisms for this observation include the release of calcium ions from lysosomes following low-level photodamage. The resulting increase in calcium ions in the cytosol initiates a calpain-mediated cleavage of ATG5, an autophagy-related protein, to a truncated, pro-apoptotic form that promotes death upon damage to mitochondria/ER [88, 102, 103]. Figure 4.12 illustrates the mechanism of dual photosensitizer-mediated phototoxicity.

The current study evaluates the efficacy of this combination PDT protocol in a 3D model that restores aspects of tumor architecture and microenvironmental cues that are not present in monolayer cultures and can influence response to therapy (e.g. gradients of nutrients and oxygen that create regions of hypoxia) [104–107]. The use of mCherry as a fluorescent reporter in 3D culture confers advantages in imaging and analysis, because external dyes for fluorescence imaging are limited by the penetration of both the light and the dye molecules in 3D tumor spheroids, which can impact their utility in the evaluation of cell viability. mCherry fluorescence is advantageous in this respect because it is expressed by all living cells in the spheroid, making it a potentially useful reporter in studies that are conducted on 3D tumor models.

The results of the present study revealed that PDT using the combination of two different liposomal formulation of BPD is more effective that the total of individual

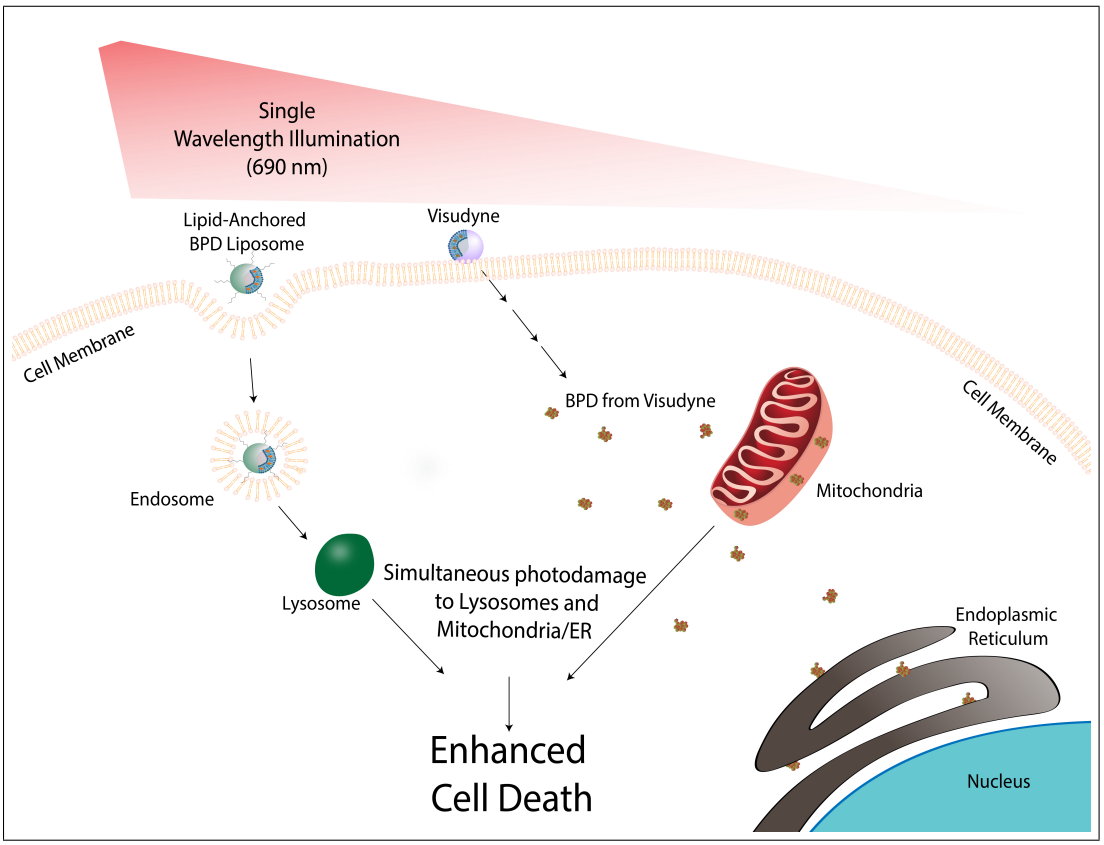

Figure 4.12 Mechanism of dual photosensitizer-mediated phototoxicity: lipid-anchored BPD liposome is taken up by the cell membrane forming an endosome, which matures into a lysosome. The free BPD from Visudyne enters the cell and localizes primarily to the mitochondria and partially to the endoplasmic reticulum. When irradiated with a single wavelength of light, the low-level lysosomal photodamage enhances mitochondrial-related cell death pathways upon initiation of mitochondrial photodamage.

therapies in a 3D tumor model. Moreover, this study successfully used mCherry expression as a cell viability reporter in a 3D tumor model for the first time. Evaluating the same PDT protocol in animal models and examining the death modes that are triggered *in vivo* as a result of photodamage to mitochondria, ER, and/or lysosomes are important next steps to determine the feasibility of this therapeutic approach beyond the current *in vitro* findings.

5. NOVEL IN VITRO MODELS TO ELUCIDATE MECHANOTRANSDUCTION-BASED TUMOR PROGRESSION, AGGRESSION AND RESISTANCE TO THERAPY: A PRELIMINARY PIT STUDY

5.1 Introduction

Despite latest research that provides an insight on tumor biology, conventional cancer treatments did not improve enough to provide an ultimate treatment. One of the reasons why more effective treatment methods cannot be developed is the lack of appropriate models that are able to simulate adequately the real biological environment and processes that occur in the human body [108]. While conventional monolayer cell cultures are useful for providing insights into several biological processes, they cannot mimic important physiological factors, such as hypoxic environment in the tumor [109]. Similarly, *in vivo* models have limitations for researchers in terms of controlling the conditions and monitoring the outcomes [110]. For this reason, developing *in vitro* models that better mimic *in vivo* conditions is crucial. Altered biophysical and mechanical properties are characteristics of tumors. Hence, tumor tissues are exposed to a number of different chemical and mechanical stimuli, which affect cancer's progression, aggression, and migratory behavior [1, 110]. A tumor microenvironment is a complex and dynamic milieu, where malignant cells are surrounded by blood vessels and other cellular and non-cellular constituents. Infiltrating immune cells, endothelial cells, fibroblasts and adipocytes, as well as the constituents of extracellular matrix (ECM) are components of the tumor microenvironment [1]. ECM has an important role for the structural and mechanical integrity of the tissue [2]. Particularly in cancer, the cells can be strongly affected by the mechanical properties of the tumor microenvironment, such as the stiffness and heterogeneity of ECM. The tumor may also be exposed to tensile, compressive or shear stresses, that are stem from certain forces or fluid flow [1, 3].

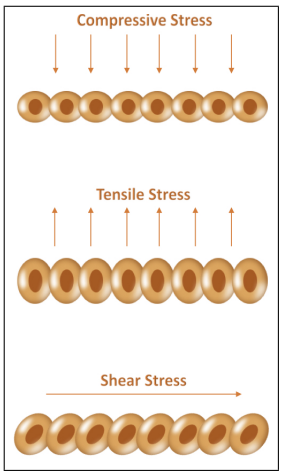

Figure 5.1 Mechanical stress types that cancer cells are exposed.

This chapter discusses the consequences of mechanical stimuli on tumors and reviews the novel *in vitro* models that have been developed for studying the microenvironmental mechanical effects in tumors. Moreover, the preliminary results of a corresponding study are introduced within the context of this chapter.

5.1.1 Mechanotransduction on cancer progression and aggression

Mechanical conditions in a tumor environment may elicit certain biological responses. The term "mechanotransduction" addresses the biological response of cells to mechanical stimuli. Recent studies have shown that physical changes are as determinant as chemicals in terms of tumor progression and aggression of cancer [1, 3, 9, 111–114]. This section addresses the potential mechanical stresses inside or around a tumor and the biological responses to these stresses.

5.1.1.1 Causes of compressive and tensile stress in tumor. Two of the essential mechanical stresses encountered in a growing tumor are the compressive and tensile stresses, which primarily originate from the increasing mass of the tumor itself and the stiffening of the extracellular matrix [3, 115, 116]. As the primary characteristics of cancer, rapid proliferation and reduced apoptosis cause an increase in the tumor

mass. The release of chemokines and growth factors by tumor-associated stromal cells, such as fibroblasts, mesenchymal stem cells and immune cells that accumulated in the tumor site, also contribute to tumor growth [1, 117]. Even if the constituents of ECM, such as collagen and water-trapped hyaluronic acid, create a resistance, the tumor growth may continue and start pressing the nearby healthy tissue, which causes the accumulation of stress [109, 115, 116, 118]. Two computational modeling studies showed that the solid stress is compressive (radial) at the interior of a growing spheroid, but it is both compressive and tensile (radial and circumferential) at the boundary [119, 120]. Tensile forces may also be induced by interstitial fluid flow. For instance, Polacheck *et al*. have shown that the tensile stress that occurs on the upstream side of the cells during a constant flow causes alterations in focal adhesions, which eventually effect the migration direction of the cells [4].

The stiffer structure comparing the surrounding tissue is also a well-known property of a tumor and this fact is the basis of palpation of cancer in soft tissue [121, 122]. The stiff architecture is caused by the increased amount of cancer cells and altered tumor ECM composition. ECM is a complex scaffold that surrounds the tissue and provides structural support [1, 2]. ECM composition and organization is determinant because cells interact with ECM via transmembrane receptor integrin, at an anchoring complex called focal adhesion, and may change their behavior accordingly [3, 123]. Focal adhesion kinase (FAK), integrin-linked kinase (ILK) and other cytoplasmic and membrane-associated proteins contribute to this interaction as key regulators and effectors of integrin [123, 124]. The stiffness of ECM not only depends on the increase but also on the augmentation in cross-linking and parallel reorienting of collagens, which are the most abundant ECM scaffolding protein [125]. The thick fiber structure of the tumor's ECM is an additional cause of pressure and stress on the tumor cells [1–3].

5.1.1.2 Consequences of compressive and tensile stress in tumor. Composition and stiffness of the extracellular matrix alter tumor cell behavior. For instance, durotaxis is the migration of cells towards the stiffer matrix. *In vitro* models that are designed to research durotaxis usually use 2D or 3D collagen gels. However, be-

cause collagen's porosity changes according to the stiffness, it is difficult to distinguish whether the effect on cell migration originates from ECM stiffness or other parameters, such as the matrix pore size and adhesive ligand density [2,126–128]. Lang *et al.* overcame this problem by using glutaraldehyde as a cross-linker to increase the stiffness of the collagen independently from its density and pore size [125]. A second alternative was suggested by Pathak *et al.* using polyacrylamide hydrogels around silicon-based scaffolds for independent variation of pore size and matrix stiffness [128]. Both studies have revealed that the migration speed of breast cancer and glioma cells is dependent on substrate stiffness. Furthermore, a novel *in vitro* platform containing a 3D tension bioreactor system that allows for the adjustment of collagen hydrogel stiffness, reported an enhanced tumor cell invasion and migration with increasing ECM stiffness [129]. Additionally, *in vivo* studies have also been performed to examine the effect of ECM stiffness on tumor progression. Among previous studies, two of them aimed to manipulate collagen cross-linking in tumor ECM by altering the Lysly oxidase amount. Both studies reported that the increased collagen cross-linking promotes tumor progression and invasion by increasing ECM stiffness, focal adhesions and PI3 kinase activity [125,130]. Similarly, the migration of tumor cells may be affected by the alignment of collagens. Alignotaxis is the rapid migration of cells along the strait aligned collagen fibers. An *in vitro* study on this topic demonstrated the relation between tumor cell migration and collagen structure [1]. External forces on the cell membrane can also lead to motility via actomyosine contraction. Actomyosine is an actin-myosine complex that enables cells to move. Increased intracellular tension through actomyosine contractility triggers certain processes such as cell proliferation, ECM remodeling, tissue polarity and eventually affects cancer cell progression and invasion [3]. There are contradictory findings regarding the effect of compressive stress on tumors. It has been showed that compressive pressure causes tumor progression, invasiveness and metastatic behavior by altering gene expression of cancer cells [111]. Additionally, the compressive stress causes the constriction of lymphatic vasculature and interstitial space, which may hinder the delivery of therapeutics and facilitate cancer cells to escape [3]. Another negative effect of compressive pressure on tumor progression is the constriction of the blood vessels. Narrowed blood and lymph vessels cause hypoxia and the decrease of the tumor microenvironment's pH level [111, 116, 118, 131]. Hypoxia in tumors is

associated with the augmented release of growth factors (TGFβ- and VEGF) and the suppression of immune cell activities [115]. Moreover, this harsh hypoxic and acidic microenvironment leads to a more resistive tumor phenotype by creating a survival advantage for more malignant cancer cells [132]. Conversely, there are studies showing that applying an external pressure on a tumor may stop cancer growth and increase apoptosis [118, 133].

5.1.1.3 Causes of shear stress in tumor. The shear stress is defined as the stress originated from applied forces in parallel to an object. In tumors, this stress is mainly caused by fluid flow. Tumor cells can be exposed to fluid flow both internally or externally. There are three main fluid flows inside a tumor; the flow along tumor vasculature (intravascular), the flow through the tumor interstitial space (interstitial), and lastly, the drainage from the lymph (lymphatic) [114]. All three fluid flow are dependent to each other, so any change in one affects the other. However, the shear stress that is caused by the interstitial fluid was found to be directly associated with tumor progression [4] Intestine, stomach or other cells of the organs in the peritoneal cavity are also exposed to certain body fluid flows [113]. Malignant ascites, the buildup of fluid inside the peritoneal cavity, is an example that may create shear stress on tumors externally. Breast, colonic, endometrial, gastric, pancreatic and ovarian cancers are associated with accumulation of ascites [5]. In a normal functioning body, ascites is drained out by the system but in pathological conditions such as cancer, the rate of fluid production may exceed the rate of clearance. Besides causing pain and dyspnea, ascites is also accepted as a sign of poor prognosis and a reason of metastasis in cancer [5].

5.1.1.4 Consequences of shear stress in tumor. Shear stress is sensed by the cells via transmembrane receptors, integrins, and associated focal adhesion proteins that serve as a mechanical link between the ECM and cytoskeleton [4, 113, 123]. These membrane-associated glycoproteins interact with signaling molecules and proteins to control certain cellular events [6]. The effects of shear stress on the progression and aggression of the cancer has been widely studied. For example, the relation between

Figure 5.2 Mechanical stimuli in tumor. The accumulation of tumor mass, stiffness of ECM, interstitial flow, and ascites flow effects tumor progression [1–8].

interstitial flow and tumor metastasis was researched by Shields *et al.* using a simple *in vitro* model [7]. Similarly, a comprehensive study of Polacheck *et al.* was conducted on MDA-MB-231 cells using a microfluidics chip [8]. The model enables the application of stable pressure gradients and fluid flow to the cells and the monitoring of the outcomes. Both studies have reported that interstitial flow increases the metastatic potential of cancer cells. Moreover, the migration of the cells in the direction of flow was mediated by CCR-7 receptor autologous chemotaxis. However, the direction of migration may change according to cell density, flow rate, FAK activation, integrin activation. Another study, focusing on the effects of peristalsis flow on colon cancer cells, revealed that shear stress may have different effects on different cell lines. More precisely, while shear stress blocks the cell cycle in SW480 cells, it stimulates proliferation in another colon cancer cell line, Caco-2 [113]. As mentioned in the previous section, ascites formation is common in some types of cancer. The relation of malignant ascites with the dissemination and invasiveness of the cancer has been a subject of recent research. For instance, a series of experiments were performed by Rizvi *et al.*, using a novel microfluidic platform to study the effect of shear stress on 3D ovarian cancer micronodules [9]. According to the results, 3D ovarian cancer micronodules, grown under continuous laminar flow, showed altered biomarker expression and tumor

morphology, indicating an increased epithelial-mesenchymal transition (EMT). More precisely, EMT increase, which is an important step in metastatic progression, was indicated by a decrease in E-caderin and an increase in vimentin. Furthermore, the same study reported the upregulation in the expression of another key biomarker associated with the aggressive and invasive phenotype, EGFR.

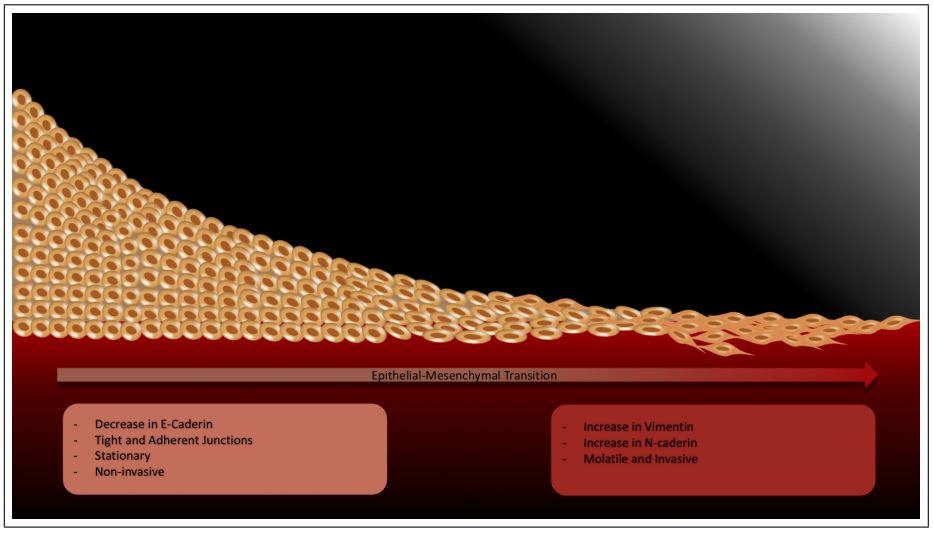

Figure 5.3 Demonstration of the epithelial-mesenchymal transition [9].

All studies above illustrate the importance of mechanical stimuli on cancer cell behavior and take advantage of the latest developments in *in vitro* models. Therefore, novel *in vitro* models that enable the mimicking of certain mechanical stresses on cancer cells have significant importance for the characterization of the disease and development of necessary treatments.

5.1.2 Novel in vitro models for studying mechanical effects on tumor progression, aggression and resistance to therapy

The most important advancement that overcomes the weakness of conventional monolayer cell cultures was the development of 3D cell culturing. Tumor spheroids obtained in 3D cultures have the required morphology to experience the oxygen and nutrient gradients similar to *in vivo*. Also, cell-to-cell and cell-to-ECM interactions that are missing in monolayer models exist in 3D tumor models [108, 110, 134], and

therefore, 3D models are very useful for studying new treatment methods. However, there are some challenges such as a lack of an ideal technique to analyze the heterogeneous tumor spheroid, because the existing methods are designed for 2D cultures. For example, the morphology of a 3D spheroid needs to be investigated by an expensive multi-photon excitation confocal microscope instead of by an optical microscope [107].

Another significant move that carries *in vitro* models a step further was the introduction of microfluidics to the field. State-of-the-art laboratories and technologies, such as cleanrooms and nanoimprint lithography, made such microfluidic platforms available for research on cultured cells. The usage of novel *in vitro* models are important for mechanotransduction studies on cancer cells because these models allow the controlled application of certain physical and chemical stimuli, as well as simultaneous monitoring [108, 110].

Table 5.1 lists the latest studies conducted on different *in vitro* platforms that investigate the mechanical effects on cancer cell behaviors.

Table 5.1
The list of novel *in vitro* models used for mechanotransduction-based cancer studies.

***In vitro* platform**	**Stress type**	**Effects on cancer cells**	**Reference**
A piston system for pushing the cancer cells that are embedded in agarose gel, towards a porous membrane.	Compressive	Cancer cell migration.	Demou *et al.* [111]
A platform consisting of a piston for compressing normal and cancer cells against a membrane.	Compressive	Invasion of cancer cells that are compressed because of tumor growth.	Tse *et al.* [112]
Cancer cells embedded in agarose gel, together with fluorescent micro-beads as markers of the strain in the gel.	Compressive	Suppressing effect of mechanical stress on tumor spheroids.	Cheng *et al.* [118]
A microfluidic platform for exposing cancer cells that are embedded to a collagen hydrogel to constant fluid flow.	Shear and tensile	Effect of interstitial fluid flow to cancer cell migration.	Polacheck *et al.* [4]
Polymerization of polyacrylamide hydrogels around silicon-based scaffolds for defined stiffness and microtopography.	Compressive	Cell migration dependence on matrix stiffness and confinement.	Lang *et al.* [127]
3D tension bioreactor system that allows for the adjustment of collagen hydrogel stiffness.	Compressive	Cell invasion and migration dependence on ECM stiffness.	Pathak *et al.* [128]
Tumor spheroids cultured on Agarose gel.	Compressive	Tumor growth inhibition because of the compressive stress accumulation.	Helmlinger *et al.* [133]
Cancer cells cultured on Matrigel containing Boyden chambers (12 mm diameter and 8 μm pore) that is pressed from the top for creating a constant speed fluid flow.	Shear	Chemotaxis and tumor cell migration.	Shields *et al.* [7]
Cells seeded in 3D collagen type I microfluidic platform that allows the application of stable pressure gradients and fluid flow.	Shear and tensile	Migration direction.	Polacheck *et al.* [8]
Microfluidic platform for 3D growth of tumor spheroids under continuous laminar flow.	Shear	Aggressiveness and Resistance of cancer cells.	Rizvi *et al.* [9]
Double layered type I collagen with micrometer-scale cavities.	Tensile	Collective cell migration.	Gjorevski *et al.* [135]
Tissue culture dishes rotated in both horizontal and vertical rotations on a lab rotator to mimic peritoneal fluid motion.	Shear	Progression, invasion and metastasis of tumor spheroids.	Hyler *et al.* [136]
A PDMS microchannel platform connected to a pumping mechanism.	Shear	Cancer cell proliferation and migration.	Das *et al.* [137]
A PDMS microfluidic platform that allows 3D cell culturing, well-controlled flow conditions and live imaging.	Shear	Invasion and migration of cancer cells in the interstitial flow direction.	Haessler *et al.* [138]
Confined microchannels and mechanical barriers for mimicking mechanical boundaries such as cell-cell junctions and dense ECM.	Compressive	Invasion and migration of cancer cells.	Mak *et al.* [139]
PDMS microchannels coated with aligned or random collagen.	Alignotaxis	Relation between collagen alignment and cancer invasion/metastasis.	Riching *et al.* [140]
A parallel plate flow chamber constructed with class coverslips and polyacrylamide substrates with different stiffness. Additionally a peristaltic pump for creating flow.	Shear	Effect of substrate rigidity on the capture of circulating tumor cells to endothelial blood cells in the bloodstream.	Ma *et al.* [141]

5.1.3 A preliminary PIT study against chemotherapy-resistant ovarian cancer cells on a novel in vitro platform

As discussed previously, mechanical stimuli from the tumor microenvironment may cause a more aggressive and resistant progression of tumors. Some important indications of aggressive tumors are EGFR overexpression and EMT. Previous research from the Hasan Laboratory using a novel microfluidic platform have revealed that ovarian cancer expresses more EGFR and shows strong indications of EMT under constant shear stress [9]. This result indicates that ovarian cancer cells grown under constant flow may develop a resistance to any treatment, such as Carboplatin, which is considered as a standard chemotherapeutic for ovarian cancer [142].

Photoimmunotherapy (PIT), which has been previously researched on micrometastatic ovarian cancer by the Hasan Laboratory research group [28, 143], is basically PDT that uses a photosensitizer-antibody conjugation for better targeting of cancer cells that are overexpressing certain proteins. The photosensitizer-Cetuximab (EGFR antibody) conjugate that is used in this PIT is called "Photoimmunoconjugate" (PIC).

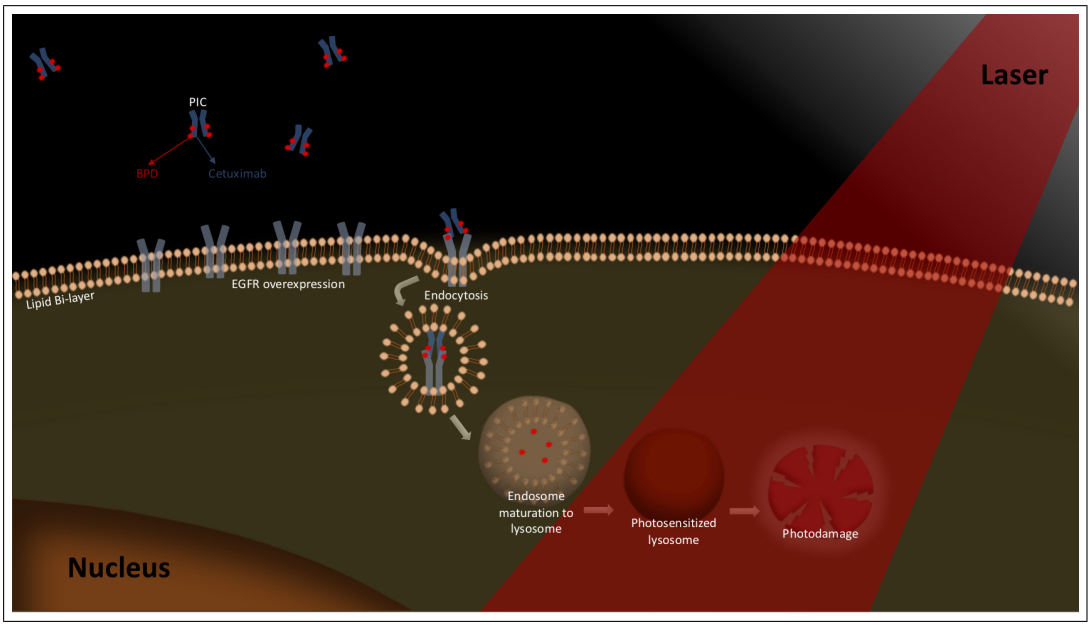

Figure 5.4 Photoimmunotherapy mechanism: Flow induces the EGFR expression in cancer cells. Photoimmunocanjugates (PIC) recognize EGFR's and binds to them. EGFR and PIC are taken into cell via endocytosis. Endosome matures to a photosensitized lysosome. Photodamage occurs with laser irradiation.

The present preliminary study uses the same microfluidic platform that was used by Rizvi *et al.* in 2013 [9], to apply PIT on ovarian cancer cells that are grown under fluidic shear stress. The aim of this study is to show PIT efficacy on chemotherapy resistant ovarian cancer micronodules.

5.2 Materials and methods

5.2.1 Cell line

Human ovarian carcinoma cells NIH:OVCAR5 (OVCAR5) were acquired from Fox Chase Cancer Center (Philadelphia, PA, USA). Cells were maintained in T75 flask at 37°C incubator with RPMI 1640 medium (Mediatech Inc., Herndon, Virginia, USA) containing 10% (v/v) heat inactivated FBS (GIBCO Life Technologies, Grand Island, New York, USA) and 1% Penicilin/Streptomycin. OVCAR5-mCherry cells were previously generated by transducing wild-type OVCAR5 with lentiviruses encoding an mCherry gene in the Hasan Laboratory [19].

5.2.2 PIC production

BPD and cetuximab were conjugated by the members of the Hasan Laboratory as described at length in a previous paper [28]. Briefly, the PEGylated cetuximab was reacted with the N-hydroxysuccinimide ester of BPD. The purification of the final PIC was performed on a Sephadex G-50 column (Amersham Pharmacia Biotech Inc., Piscataway, NJ) or a Zeba spin desalting column (ThermoScientific Rockford, IL). The purity of the resulting PIC was determined using gel electrophoresis (Ready Gel 5% Tris-HCl, Bio-Rad Laboratories). The photosensitizer content of the PIC was determined by using absorbance spectroscopy at 690 nm. The protein content of PIC was measured using a BCA protein assay (Pierce, Rockford, IL) to calculate the molar ratio of photosensitizer to EGFR antibody. The typical molar ratio of photosensitizer and antibody (PS:mAb) was 6:1 or 7:1.

5.2.3 Microfluidic chip production

The flow model procedure used in this study is the replication of a previously developed and published work of the Hasan Laboratory [9]. Microfluidic chip and other parameters such as flow rate and cell concentration were formerly optimized by Dr. Rizvi and the members of the Hasan Laboratory to evaluate the effects of treatments on ovarian cancer cells in 3D, under flow conditions. The chip was built following the previously published method [9]. Briefly, a glass coverslip was adhered to one side of a double-sided adhesive (DSA) with three channels cut out. GFR Matrigel (Corning) was distributed throughout the channels on the surface of the coverslip and PMMA was placed on the other adherent side of the DSA. Silicone tubing was inserted into holes in the PMMA and then, the cells and the medium were pumped through the tubing onto the glass coverslip and out through the outlet tubing.

5.2.4 Experiment details and timelines

In this experiment, cells grown in static conditions or under a continuous laminar flow, were treated with PIT. PIT components were as follows:

PIC: BPD equivalent concentration of 1.0 μM

Laser Irradiation: 690 nm diode laser (Model 7404, Intense Inc., North Brunswick, NJ) at an irradiance of 50 mW/cm^2 for 300 seconds.

5.2.4.1 Flow model. Cells were prepared at a concentration of 10^6 cells/ml in 1 ml syringes on day 0. Syringes were connected to the inlet tubes of the experiment chip and then placed into a syringe-pump. Cell suspensions were pumped through the inlet tubes with a rate of 100 μl/min until the cell suspensions reach the channels. 1 ml syringes were changed with 20 ml syringes that contained 20 ml of 2% GFR Matrigel in growth medium. Pumps were started at a rate of 2 μl/min and the whole system

was placed to the incubator. On day 6, syringes were replaced with PIC containing syringes for 24 hours. For PIT application, the experiment chip was irradiated with a 690 nm laser at laser energy density of 15 J/cm^2 on day 7. Cell viability was assessed on day 11.

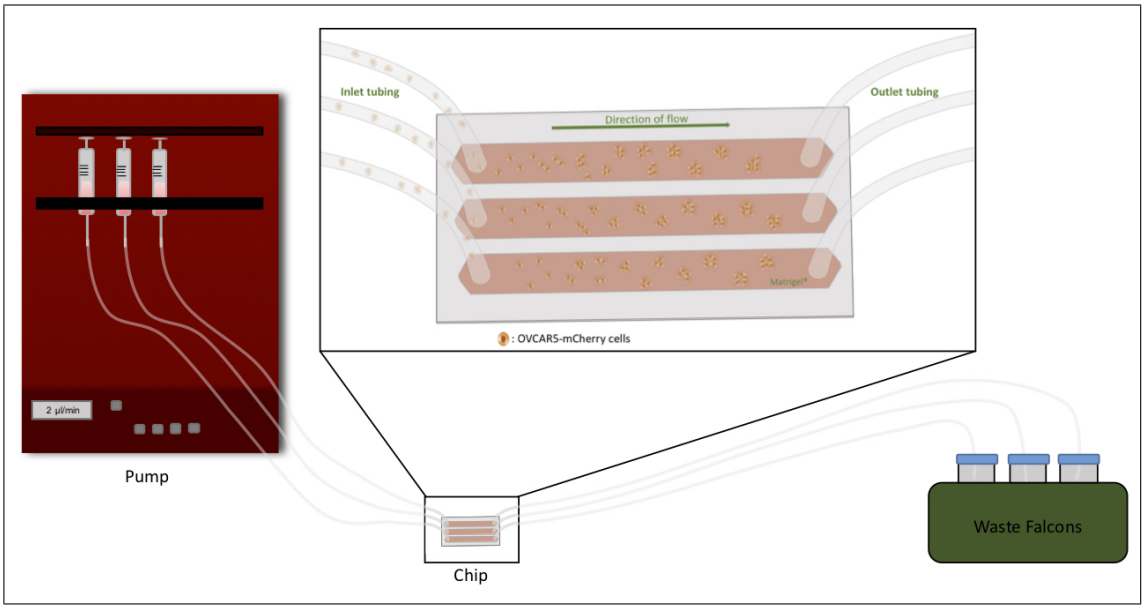

Figure 5.5 Experimental setup and microfluidic chip. Cell suspension and growth medium is pumped through silicon tubes and channels.

5.2.4.2 Static model. On day 0, cells were cultured in 3D on GFR Matrigel beds as described previously [19]. In brief, 250 μl of Matrigel was added to each well of a pre-chilled Krystal 24-well, black-wall microplate. Following 20-25 minutes of incubation at 37°C for Matrigel polymerization, the cells were plated at a density of 10,000 cells/well in 1 ml of 2% Matrigel-containing complete growth medium. The medium was refreshed on day 3. The cells were incubated with PIC on day 6 for 24 hours. For PIT application, the experiment group was irradiated with a 690nm laser at laser energy density of 15 J/cm^2 on day 7. Plates were maintained until day 11 and imaged.

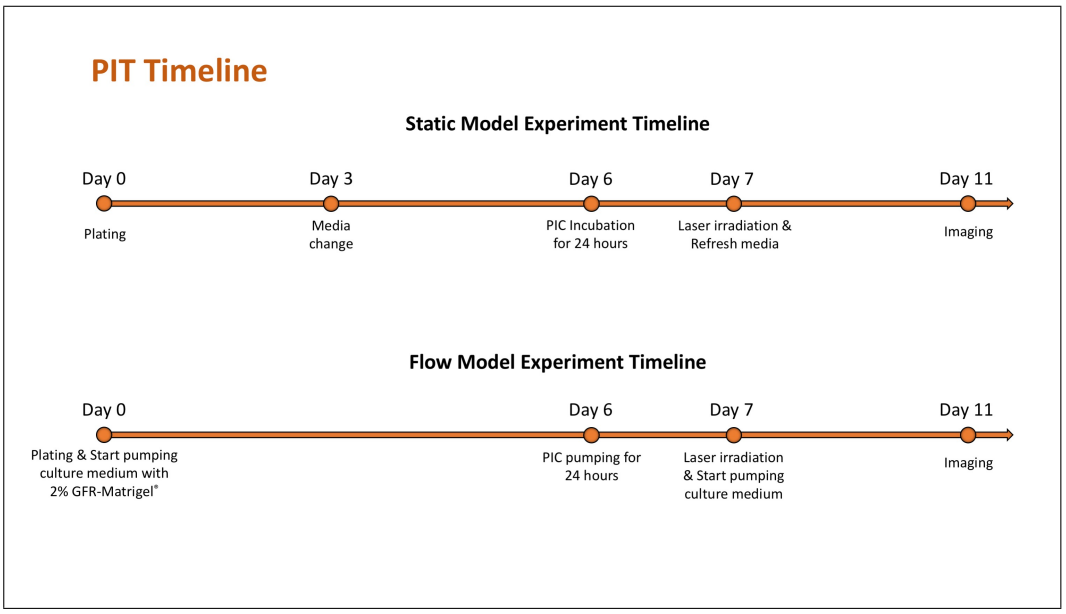

Figure 5.6 PIT experiment timeline.

5.2.5 Imaging

5.2.5.1 Flow model imaging. Tumor micronodules were imaged using an Olympus FV1000 confocal microscope. Multi-area mosaics from multiple z-stacks were obtained with a 10X objective (N.A. of 0.40). For mCherry fluorescence-mediated cell viability analysis, a channel other than bight-field was set by combining excitation and emission filters appropriate for mCherry fluorescence. Images from channels were acquired via confocal microscope using appropriate light sources and filters. The images were stitched together and processed using custom routines developed in the MATLAB software package.

5.2.5.2 Static model imaging. Cell viability was evaluated by measuring mCherry fluorescence that is emitted from live cells as described previously [19]. For mCherry fluorescence-mediated cell viability analysis, the excitation and emission spectrums of BPD and mCherry were compared to make sure that there were no undesired cross-excitations. Then, mCherry fluorescence was detected using the excitation LED (530-560 nm) and emission filter (570-650 nm) of Operetta CLS High Content Image Analysis System (Perkin Elmer). Images were acquired using 5X air objective lens (N.A.

of 0.16) in multiple z-stacks (between 10-14) with 50 μm step size. During imaging, the chamber of the system was kept at 37°C with 5% CO_2. Acquired images were analyzed using Harmony 4.6 software (Perkin Elmer). In brief, image mosaics were joined together for each plane and every z-plane images were combined to construct a final 2-dimensional image for each well. A threshold for mCherry fluorescence was determined at the beginning of each analysis based on the "No Treatment Control" to establish the "Live Tumor Area".

5.2.6 Statistics

Each experiment was repeated at least three times. All values were normalized to the "No Treatment Control" group and were presented as a fraction of the no treatment tumor area. Unpaired t-test was used to compare both the controls with the treatment groups and the two treatment groups with each other.

5.3 Results

High EGFR expression is one of the poor clinical outcomes in ovarian cancer, which is associated with increased proliferation and survival. It has been shown that fluidic shear stress causes increased expression and activation of cell-surface receptor EGFR in ovarian cancer cells [9]. Additionally, a recent research has revealed that fluid shear stress increases resistance to chemotherapy in ovarian cancer [144]. In this study, our aim was to show that in contrast to chemotherapy, ovarian cancer cells grown under fluidic shear stress are not resistant to PIT. The results did not show any statistically significant difference in terms of viable tumor area between the static and flow models (Figure 5.7). In conclusion, PIT treatment is not negatively affected by the fluidic shear stress. This result supports the argument that photochemistry can be used to kill chemotherapy resistant cancer cells.

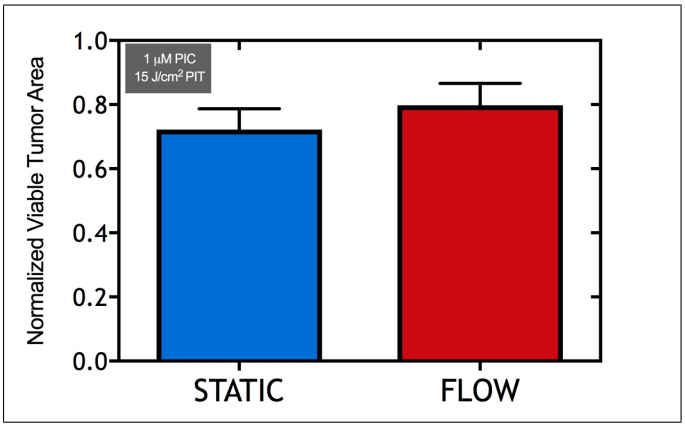

Figure 5.7 Results of the PIT experiment. Viable tumor areas were normalized to respective no treatment controls.

5.4 Discussion and future directions

The exposure of cancer cells to certain mechanical stresses may change their properties and activities. Compressive and shear stress that have occurred in tumor microenvironments may induce a more resistant and invasive cancer cell behavior. Therefore, the examination of these effects and the development of appropriate treatments is crucial. Due to the developments in the cell culturing techniques and microflu-

idics, the new *in vitro* models that enable mechanotransduction studies on cancer cells are being designed. For example, a novel experiment platform was designed to create solid stress on cancer cells by embedding them in agarose gel [118]. In this model, fluorescent micro-beads were used as markers of the strain in the gel. Another 3D platform was constructed using collagen for examining the collective cell migration. The article reports that the tensile forces drive collective cell migration through micro-cracks that were created by leading fibroblasts [135]. The common finding of these of mechanotransduction studies are increased invasiveness, migration and resistance to chemotherapy of cancer cells [7–9, 128–132, 135–139]. Conversely, there are findings stating that compressive stress may cause a decrease in cancer cell viability [118, 133]. Ovarian cancer is one of the most affected cancer type from the mechanical conditions. In the peritoneal cavity, ovarian cancer cells are constantly undergoing certain stresses, such as the shear stress, stemming from ascites build-up. The increase in the survival, resistance and invasiveness of ovarian cancer cells under shear stress has been previously studied. For example, a recent study of Hyler *et al.* illustrated that the benign ovarian cells revealed morphological changes and chromosomal instability under fluid shear stress. Furthermore, the shear stress promotes anchorage-independent survival of cancer cells, which might be associated with the invasion and metastasis of the cancer [136]. Another study of Rizvi *et al.* showed that ovarian cancer cells tend to increase EMT under fluid shear stress, which is associated with a more aggressive and invasive phenotype [9].

A list of the relevant novel *in vitro* models and their significance in the literature has been presented in Table 5.1. The majority of the platforms that are designed to investigate the compressive stress on cancer cells use certain 3D gels that are mimicking the stiff extracellular matrix. These materials serve as either an environmental matrix with stiffness gradients, guiding tracks for migrating cells or simply obstacles that are inhibiting tumor spheroid growth. Another group of novel *in vitro* platforms mainly consists of micro-cavities or channels to study shear stress and the migration direction of cancer cells. One of the *in vitro* platforms listed in Table 5.1 was designed and developed by the Hasan Laboratory for studying micrometastatic ovarian cancer under continuous laminar flow [9]. The same model was used in the preliminary study that

was presented within the context of this chapter. In this study, OVCAR5-mCherry cells were grown under static or flowing growth medium and treated by PIT. OVCAR5-mCherry cells have the unique property of emitting mCherry fluorescence while they are alive, which enables us to collect cell viability data directly from the entire cancer micronodules, including the inner regions [19]. Research has shown that cancer cells that have been cultured on a microfluidic platform and exposed to constant medium flow show different properties compared to the cells grown in static growth medium [9]. For instance, the cells in the flow model show resistance to chemotherapy [144]. As an alternative treatment modality, a photochemical approach, PIT, has been studied on both static and flow *in vitro* models. The results indicate that ovarian cancer cells in the microfluidic platform had not shown a significant resistant to PIT at low doses. This outcome reveals the potential of PIT on the aggressive and resistant ovarian cancer micronodules; however, the effect on cancer cells at higher PIT dose products should be explored.

Concerning the future studies, we are planning to use the same microfluidic platform to compare chemotherapy and PIT at higher dose products. Moreover, low-dose PIT will be applied before chemotherapy for priming purposes. Our expectation is that the PIT application prior to chemotherapy will prime the resistant micronodules and provide an enhanced cancer cell killing at very low doses of chemotherapy.

6. CONCLUSION

Despite the advancement and success over the past decades, the photochemical cancer treatment approach PDT is still being researched for increased efficacy and effective use in clinical oncology [145]. The three major studies that were presented in the context of this thesis were designed to propose and to test different PDT strategies. Performing these studies on different *in vitro* models also enabled the evaluation, discussion and acknowledgement of the importance of conventional and complex *in vitro* models in cancer research.

The first study of this PhD research evaluates the potential of the FDA-approved dye ICG, which is primarily used for imaging purposes in clinics, as a PDT agent. ICG is advantageous as a photosensitizer due to its strong absorbance at the near-infrared region of electromagnetic spectrum; however, the debate is still open as to whether ICG's mechanism of action is photothermal or photochemical. Furthermore, the aggregation of ICG in aqueous solutions, and how this problem affects ICG's efficacy, has not been conclusively evaluated by researchers. Addressing this gap, the first study was conducted on conventional cell cultures of three different human cancer cell lines. The assessment of the results revealed that ICG is an effective PDT agent over certain concentrations and that the laser energy density level used in the application determines whether the major reaction is photothermal or photochemical. This study also provided quantitative data on how the problem of aggregation affects the singlet oxygen quantum yield of ICG.

The aim of the second study was to increase PDT efficacy by targeting different organelles in cancer cells. Research has shown that the sequential or simultaneous damage to different organelles enhances PDT [89–91]. In this study, two liposomal formulations of BPD that are preferentially localized on mitochondria, ER and lysosomes, were activated simultaneously by 690 nm laser. The results revealed that this strategy increases the efficacy of PDT on 3D cancer nodules.

The last major chapter of this dissertation focuses on the importance of mechanical effects on tumor progression and reviews novel *in vitro* platforms that mimic those mechanical stimuli. Furthermore, a preliminary study that was conducted on a novel *in vitro* platform was presented. The aim of the study is to show that the ovarian cancer spheroids, which show resistivity to chemotherapy under constant medium flow, can be efficiently killed by PIT. According to the results, PIT at low doses is equally effective on both static and flow models, which reveals that PIT can be considered as an alternative for chemotherapy-resistant ovarian cancer.

To conclude, this PhD research achieved its objectives by contributing to the literature on photochemical treatment of cancer and by providing a basis for various follow-up studies.

REFERENCES

1. Oudin, M. J., and V. M. Weaver, "Physical and chemical gradients in the tumor microenvironment regulate tumor cell invasion, migration, and metastasis," *Cold Spring Harbor Symposia on Quantitative Biology*, Vol. 81, no. 1, pp. 189–205, 2016.

2. Malandrino, A., M. Mak, R. D. Kamm, and E. Moeendarbary, "Complex mechanics of the heterogeneous extracellular matrix in cancer," *Extreme Mechanics Letters*, Vol. 21, pp. 25–34, 2018.

3. Northcott, J. M., I. S. Dean, J. K. Mouw, and V. M. Weaver, "Feeling Stress: The Mechanics of Cancer Progression and Aggression," *Frontiers in Cell and Developmental Biology*, Vol. 6, no. February, pp. 1–12, 2018.

4. Polacheck, W. J., A. E. German, A. Mammoto, D. E. Ingber, and R. D. Kamm, "Mechanotransduction of fluid stresses governs 3D cell migration," *Proceedings of the National Academy of Sciences*, Vol. 111, no. 7, pp. 2447–2452, 2014.

5. Adam, R. A., and Y. G. Adam, "Malignant ascites: Past, present, and future," *Journal of the American College of Surgeons*, Vol. 198, no. 6, pp. 999–1011, 2004.

6. Shyy, J. Y. J., and S. Chien, "Role of integrins in endothelial mechanosensing of shear stress," *Circulation Research*, Vol. 91, no. 9, pp. 769–775, 2002.

7. Shields, J. D., M. E. Fleury, C. Yong, A. A. Tomei, G. J. Randolph, and M. A. Swartz, "Autologous Chemotaxis as a Mechanism of Tumor Cell Homing to Lymphatics via Interstitial Flow and Autocrine CCR7 Signaling," *Cancer Cell*, Vol. 11, no. 6, pp. 526–538, 2007.

8. Polacheck, W. J., J. L. Charest, and R. D. Kamm, "Interstitial flow influences direction of tumor cell migration through competing mechanisms," *Proceedings of the National Academy of Sciences*, Vol. 108, no. 27, pp. 11115–11120, 2011.

9. Rizvi, I., U. A. Gurkan, S. Tasoglu, N. Alagic, J. P. Celli, L. B. Mensah, Z. Mai, U. Demirci, and T. Hasan, "Flow induces epithelial-mesenchymal transition, cellular heterogeneity and biomarker modulation in 3D ovarian cancer nodules," *PNAS*, pp. E1974–E1983, 2013.

10. Nyst, H. J., I. B. Tan, F. A. Stewart, and A. J. Balm, "Is photodynamic therapy a good alternative to surgery and radiotherapy in the treatment of head and neck cancer?," *Photodiagnosis and Photodynamic Therapy*, Vol. 6, no. 1, pp. 3–11, 2009.

11. Spring, B. Q., I. Rizvi, N. Xu, T. Hasan, M. G. Hospital, H. Medical, and S. E. Hospital, "The role of photodynamic therapy in overcoming cancer drug resistance," *Photochemistry and Photobiology*, Vol. 14, no. 8, pp. 1476–1491, 2016.

12. Gyenge, E. B., P. Forny, D. Lüscher, A. Laass, H. Walt, and C. Maake, "Effects of hypericin and a chlorin based photosensitizer alone or in combination in squamous cell carcinoma cells in the dark," *Photodiagnosis and Photodynamic Therapy*, Vol. 9, no. 4, pp. 321–331, 2012.

13. Huang, H. C., I. Rizvi, J. Liu, S. Anbil, A. Kalra, H. Lee, Y. Baglo, N. Paz, D. Hayden, S. Pereira, B. W. Pogue, J. Fitzgerald, and T. Hasan, "Photodynamic priming mitigates chemotherapeutic selection pressures and improves drug delivery," *Cancer Research*, Vol. 78, no. 2, pp. 558–571, 2018.

14. Rizvi, I., J. P. Celli, C. L. Evans, A. O. Abu-Yousif, A. Muzikansky, B. W. Pogue, D. Finkelstein, and T. Hasan, "Synergistic enhancement of carboplatin efficacy with photodynamic therapy in a three-dimensional model for micrometastatic ovarian cancer," *Cancer Research*, 2010.

15. Colasanti, A., A. Kisslinger, M. Quarto, and P. Riccio, "Combined effects of radiotherapy and photodynamic therapy on an in vitro human prostate model," *Acta Biochimica Polonica*, Vol. 51, no. 4, pp. 1039–1046, 2004.

16. Agostinis, P., K. Berg, K. A. Cengel, T. H. Foster, A. W. Girotti, S. O. Gollnick, S. M. Hahn, M. R. Hamblin, A. Juzeniene, D. Kessel, M. Korbelik, J. Moan, P. Mroz, D. Nowis, J. Piette, B. Wilson, and J. Golab, "Photodynamic Therapy of Cancer: An Update," *CA: A Cancer Journal for Clinicians*, Vol. 61, pp. 250–281, 2011.

17. van Straten, D., V. Mashayekhi, H. S. de Bruijn, S. Oliveira, and D. J. Robinson, "Oncologic photodynamic therapy: Basic principles, current clinical status and future directions," *Cancers*, Vol. 9, no. 2, pp. 1–54, 2017.

18. Ruhi, M., A. Ak, and M. Gülsoy, "Dose-dependent photochemical/photothermal toxicity of indocyanine green-based therapy on three different cancer cell lines," *Photodiagnosis and Photodynamic Therapy*, Vol. 21, 2018.

19. Rizvi, I., S. Nath, G. Obaid, M. K. Ruhi, K. Moore, S. Bano, D. Kessel, and T. Hasan, "A Combination of Visudyne and a Lipid-anchored Liposomal Formulation of Benzoporphyrin Derivative Enhances Photodynamic Therapy Efficacy in a 3D Model for Ovarian Cancer," *Photochemistry and Photobiology*, Vol. 95, pp. 419–429, 2019.

20. Shirata, C., J. Kaneko, Y. Inagaki, T. Kokudo, M. Sato, S. Kiritani, N. Akamatsu, J. Arita, Y. Sakamoto, K. Hasegawa, and N. Kokudo, "Near-infrared photothermal/photodynamic therapy with indocyanine green induces apoptosis of hepatocellular carcinoma cells through oxidative stress," *Scientific Reports*, Vol. 7, no. 1, pp. 1–8, 2017.

21. Castano, A. P., T. N. Demidova, and M. R. Hamblin, "Mechanisms in photodynamic therapy: Part one - Photosensitizers, photochemistry and cellular localization," *Photodiagnosis and Photodynamic Therapy*, Vol. 1, no. 4, pp. 279–293, 2004.

22. Lucky, S. S., K. C. Soo, and Y. Zhang, "Nanoparticles in photodynamic therapy," *Chemical Reviews*, Vol. 115, no. 4, pp. 1990–2042, 2015.

23. Kessel, D., "Photodynamic therapy: From the beginning," *Photodiagnosis and Photodynamic Therapy*, Vol. 1, no. 1, pp. 3–7, 2004.

24. Josefsen, L. B., and R. W. Boyle, "Photodynamic therapy and the development of metal-based photosensitisers," *Metal-Based Drugs*, Vol. 2008, 2008.

25. Kou, J., D. Dou, and L. Yang, "Porphyrin photosensitizers in photodynamic therapy and its applications," *Oncotarget*, Vol. 8, no. 46, pp. 81591–81603, 2017.

26. Allison, R. R., G. H. Downie, R. Cuenca, X. H. Hu, C. J. Childs, and C. H. Sibata, "Photosensitizers in clinical PDT," *Photodiagnosis and Photodynamic Therapy*, Vol. 1, no. 1, pp. 27–42, 2004.

27. Hamblin, M. R., and P. Mroz, *Advances in Photodynamic Therapy: Basic, Translational, and Clinical*, Artech House, 2008.

28. Abu-Yousif, A. O., A. C. E. Moor, X. Zheng, M. D. Savellano, W. Yu, P. K. Selbo, and T. Hasan, "Epidermal Growth Factor Receptor-Targeted Photosensitizer Selectively Inhibits EGFR Signaling and Induces Targeted Phototoxicity In Ovarian Cancer Cells," *Cancer Letters*, Vol. 321, no. 2, pp. 120–127, 2012.

29. Abrahamse, H., M. R. Hamblin, S. Africa, and M. G. Hospital, "New photossensitizersfot photodynamic therapy," *Biochemical Journal*, Vol. 473, no. 4, pp. 347–364, 2017.

30. Solban, N., I. Rizvi, and T. Hasan, "Targeted photodynamic therapy," *Lasers in Surgery and Medicine*, Vol. 38, no. 5, pp. 522–531, 2006.

31. Reiners, J. J., J. A. Caruso, P. Mathieu, B. Chelladurai, X.-M. Yin, and D. Kessel, "Release of cytochrome c and activation of pro-caspase-9 following lysosomal photodamage involves bid cleavage," *Cell Death and Differentiation*, Vol. 9, no. 9, pp. 934–944, 2002.

32. Kessel, D., and C. L. Evans, "Promotion of Proapoptotic Signals by Lysosomal Photodamage: Mechanistic Aspects and Influence of Autophagy," *Photochemistry and Photobiology*, Vol. 92, pp. 620–623, 2016.

33. Giraudeau, C., A. Moussaron, A. Stallivieri, S. Mordon, and C. Frochot, "Indocyanine Green: Photosensitizer or Chromophore? Still a Debate," *Current Medicinal Chemistry*, Vol. 21, no. 16, pp. 1871–1897, 2014.

34. Saxena, V., M. Sadoqi, and J. Shao, "Degradation kinetics of indocyanine green in aqueous solution," *Journal of Pharmaceutical Sciences*, Vol. 92, no. 10, pp. 2090–2097, 2003.

35. Philip, R., A. Penzkofer, W. Bäumler, R. M. Szeimies, and C. Abels, "Absorption and fluorescence spectroscopic investigation of indocyanine green," *Journal of Photochemistry and Photobiology A: Chemistry*, Vol. 96, no. 1-3, pp. 137–148, 1996.

36. Engel, E., R. diger Schraml, T. Maisch, K. Kobuch, B. Konig, R.-M. Szeimies, J. Hillenkamp, W. Baumler, and R. Vasold, "Light-induced decomposition of indocyanine green," *Investigative Ophthalmology & Visual Science*, Vol. 49, no. 5, pp. 1777–1783, 2008.

37. Mamoon, A. M., A. M. Gamal-Eldeen, M. E. Ruppel, R. J. Smith, T. Tsang, and L. M. Miller, "In vitro efficiency and mechanistic role of indocyanine green as photodynamic therapy agent for human melanoma," *Photodiagnosis and Photodynamic Therapy*, Vol. 6, no. 2, pp. 105–116, 2009.

38. Abels, C., S. Fickweiler, P. Weiderer, W. Bäumler, F. Hofstädter, M. Landthaler, and R. M. Szeimies, "Indocyanine green (ICG) and laser irradiation induce photooxidation," *Archives of Dermatological Research*, Vol. 292, no. 8, pp. 404–411, 2000.

39. Bäumler, W., C. Abels, S. Karrer, T. Weiß, H. Messmann, M. Landthaler, and R.-M. Szeimies, "Photo-oxidative killing of human colonic cancer cells using indocyanine green and infrared light," *British Journal of Cancer*, Vol. 80, no. November 1998, pp. 360–363, 1999.

40. Topaloglu, N., M. Guney, N. Aysan, M. Gulsoy, and S. Yuksel, "The role of reactive oxygen species in the antibacterial photodynamic treatment: Photoinactivation vs proliferation," *Letters in Applied Microbiology*, Vol. 62, no. 3, pp. 230–236, 2016.

41. Fickweiler, S., R.-M. Szeimies, W. Bäumler, P. Steinbach, S. Karrer, A. E. Goetz, C. Abels, and F. Hofstädter, "Indocyanine green: intracellular uptake and phototherapeutic effects in vitro," *Journal of Photochemistry and Photobiology B: Biology*, Vol. 38, no. 2-3, pp. 178–183, 1997.

42. Tang, Y., and A. J. McGoron, "Combined effects of laser-ICG photothermotherapy and doxorubicin chemotherapy on ovarian cancer cells," *Journal of Photochemistry and Photobiology B: Biology*, Vol. 97, no. 3, pp. 138–144, 2009.

43. Kranz, S., M. Huebsch, A. Guellmar, A. Voelpel, S. Tonndorf-Martini, and B. W. Sigusch, "Antibacterial photodynamic treatment of periodontopathogenic bacteria with indocyanine green and near-infrared laser light enhanced by TroloxTM," *Lasers in Surgery and Medicine*, Vol. 47, no. 4, pp. 350–360, 2015.

44. Yan, F., H. Wu, H. Liu, Z. Deng, H. Liu, W. Duan, X. Liu, and H. Zheng, "Molecular imaging-guided photothermal/photodynamic therapy against tumor by iRGD-modified indocyanine green nanoparticles," *Journal of Controlled Release*, Vol. 224, pp. 217–228, 2016.

45. Jian, W. H., T. W. Yu, C. J. Chen, W. C. Huang, H. C. Chiu, and W. H. Chiang, "Indocyanine Green-Encapsulated Hybrid Polymeric Nanomicelles for Photothermal Cancer Therapy," *Langmuir*, Vol. 31, no. 22, pp. 6202–6210, 2015.

46. Shafirstein, G., D. Sc, W. Bäumler, L. J. Hennings, E. R. Siegel, R. Friedman, M. A. Moreno, J. Webber, C. Jackson, and J. Robert, "Indocyanine Green Enhanced Near Infrared Laser Treatment of Murine Mammary Carcinoma," *International Journal of Cancer*, Vol. 130, no. 5, pp. 1208–1215, 2013.

47. Kosaka, N., M. Mitsunaga, M. R. Longmire, P. L. Choyke, and H. Kobayashi, "Near infrared fluorescence-guided real-time endoscopic detection of peritoneal ovarian cancer nodules using intravenously injected indocyanine green," *International Journal of Cancer*, Vol. 129, no. 7, pp. 1671–1677, 2011.

48. Martirosyan, N. L., D. D. Cavalcanti, J. M. Eschbacher, P. M. Delaney, A. C. Scheck, M. G. Abdelwahab, P. Nakaji, R. F. Spetzler, and M. C. Preul, "Use of in vivo near-infrared laser confocal endomicroscopy with indocyanine green to detect the boundary of infiltrative tumor," *Journal of Neurosurgery*, Vol. 115, no. 6, pp. 1131–1138, 2011.

49. Tummers, Q. R., C. E. Hoogstins, A. A. Peters, C. D. De Kroon, J. B. M. Trimbos, C. J. Van De Velde, J. V. Frangioni, A. L. Vahrmeijer, and K. N. Gaarenstroom, "The value of intraoperative near-infrared fluorescence imaging based on enhanced permeability and retention of indocyanine green: Feasibility and false-positives in ovarian cancer," *PLoS ONE*, Vol. 10, no. 6, pp. 1–12, 2015.

50. Abels, C., "Targeting of the vascular system of solid tumours by photodynamic therapy (PDT)," *Photochemical and Photobiological Sciences*, Vol. 3, no. 8, pp. 765–771, 2004.

51. Onda, N., M. Kimura, T. Yoshida, and M. Shibutani, "Preferential tumor cellular uptake and retention of indocyanine green for in vivo tumor imaging," *International Journal of Cancer*, Vol. 139, no. 3, pp. 673–682, 2016.

52. Tseng, W. W., R. E. Saxton, A. Deganutti, and C. D. Liu, "Infrared laser activation of indocyanine green inhibits growth in human pancreatic cancer," *Pancreas*, Vol. 27, no. 3, pp. e42–e45, 2003.

53. Abo-Zeid, M. A., T. Liehr, S. M. El-Daly, A. M. Gamal-Eldeen, M. Glei, A. Shabaka, S. Bhatt, and A. Hamid, "Molecular cytogenetic evaluation of the efficacy of photodynamic therapy by indocyanine green in breast adenocarcinoma MCF-7 cells," *Photodiagnosis and Photodynamic Therapy*, Vol. 10, no. 2, pp. 194–202, 2013.

54. Urbanska, K., B. Romanowska-Dixon, Z. Matuszak, J. Oszajca, P. Nowak-Sliwinska, and G. Stochel, "Indocyanine green as a prospective sensitizer for photodynamic therapy of melanomas.," *Acta Biochimica Polonica*, Vol. 49, no. 2, pp. 387–391, 2002.

55. Lim, H. J., and C. H. Oh, "Indocyanine green-based photodynamic therapy with 785nm light emitting diode for oral squamous cancer cells," *Photodiagnosis and Photodynamic Therapy*, Vol. 8, no. 4, pp. 337–342, 2011.

56. Ruhi, M., A. Ak, and M. Gülsoy, "Efficiency of photodynamic therapy using indocyanine green and infrared light on MCF-7 breast cancer cells in vitro," in *SPIE Photonics West*, Vol. 9694, 2016.

57. Bozkulak, O., R. F. Yamaci, O. Tabakoglu, and M. Gulsoy, "Photo-toxic effects of 809-nm diode laser and indocyanine green on MDA-MB231 breast cancer cells," *Photodiagnosis and Photodynamic Therapy*, Vol. 6, no. 2, pp. 117–121, 2009.

58. Ak, A., O. Kaya, D. Cosan, and M. Gulsoy, "Indocyanine green-mediated photodynamic therapy on glioblastoma cells in vitro," *Applied Mathematics, Electronics and Computers*, Vol. 3, no. 2, pp. 133–135, 2015.

59. Zuluaga, M.-F., N. Sekkat, D. Gabriel, H. van den Bergh, and N. Lange, "Selective Photodetection and Photodynamic Therapy for Prostate Cancer through Targeting of Proteolytic Activity," *Molecular Cancer Therapeutics*, Vol. 12, no. 3, pp. 306–313, 2013.

60. Arumainayagam, N., C. M. Moore, H. U. Ahmed, and M. Emberton, "Photodynamic therapy for focal ablation of the prostate," *World Journal of Urology*, Vol. 28, no. 5, pp. 571–576, 2010.

61. Moore, C. M., M. Emberton, and S. G. Bown, "Photodynamic therapy for prostate cancer-an emerging approach for organ-confined disease," *Lasers in Surgery and Medicine*, Vol. 43, no. 7, pp. 768–775, 2011.

62. Johnson, E., S. M. Dean, and P. M. Sondel, "Antibody-based immunotherapy in high-risk neuroblastoma," *Expert Reviews in Molecular Medicine*, Vol. 9, no. 34, pp. 1–21, 2007.

63. Barron, G. A., H. Moseley, and J. A. Woods, "Differential sensitivity in cell lines to photodynamic therapy in combination with ABCG2 inhibition," *Journal of Photochemistry and Photobiology B: Biology*, Vol. 126, pp. 87–96, 2013.

64. Landsman, M. L., G. Kwant, G. al Mook, and W. G. Zijlstra, "Light-absorbing properties, stability, and spectral stabilization of indocyanine green," *Journal of Applied Physiology*, Vol. 40, no. 4, pp. 575–583, 1976.

65. Sheng, Z., D. Hu, M. Xue, M. He, P. Gong, and L. Cai, "Indocyanine green nanoparticles for theranostic applications," *Nano-Micro Letters*, Vol. 5, no. 3, pp. 145–150, 2013.

66. Quan, B., K. Choi, Y. H. Kim, K. W. Kang, and D. S. Chung, "Near infrared dye indocyanine green doped silica nanoparticles for biological imaging," *Talanta*, Vol. 99, pp. 387–393, 2012.

67. Kuo, W. S., Y. T. Chang, K. C. Cho, K. C. Chiu, C. H. Lien, C. S. Yeh, and S. J. Chen, "Gold nanomaterials conjugated with indocyanine green for dual-modality photodynamic and photothermal therapy," *Biomaterials*, Vol. 33, no. 11, pp. 3270–3278, 2012.

68. Shemesh, C. S., C. W. Hardy, D. S. Yu, B. Fernandez, and H. Zhang, "Indocyanine green loaded liposome nanocarriers for photodynamic therapy using human triple negative breast cancer cells," *Photodiagnosis and Photodynamic Therapy*, Vol. 11, no. 2, pp. 193–203, 2014.

69. Zhou, J. F., "Aggregation and degradation of indocyanine green," *Proceedings of SPIE*, Vol. 2128, no. 1, pp. 495–505, 1994.

70. Wang, P., F. Qin, Z. Zhang, and W. Cao, "Quantitative monitoring of the level of singlet oxygen using luminescence spectra of phosphorescent photosensitizer," *Optics Express*, Vol. 23, no. 18, p. 22991, 2015.

71. Arunkumar, E., P. K. Sudeep, P. V. Kamat, B. C. Noll, and B. D. Smith, "Singlet oxygen generation using iodinated squaraine and squaraine-rotaxane dyes," *New Journal of Chemistry*, Vol. 31, no. 5, pp. 677–683, 2007.

72. Han, J., H. Xia, Y. Wu, S. N. Kong, A. Deivasigamani, R. Xu, K. M. Hui, and Y. Kang, "Single-layer MoS2 nanosheet grafted upconversion nanoparticles for near-infrared fluorescence imaging-guided deep tissue cancer phototherapy," *Nanoscale*, Vol. 8, no. 15, pp. 7861–7865, 2016.

73. Wang, H., X. Yang, W. Shao, S. Chen, J. Xie, X. Zhang, J. Wang, and Y. Xie, "Ultrathin Black Phosphorus Nanosheets for Efficient Singlet Oxygen Generation," *Journal of the American Chemical Society*, Vol. 137, no. 35, pp. 11376–11382, 2015.

74. Qing-luan, L. Ü., Y. U. E. Ning-ning, Z. Miao, G. Bin, and W. Huai-you, "Capacity of Tea Scavenging Singlet Oxygen Studied by Means of 1 , 3-Diphenylisobenzofuran as Fluorescence Probe," *Chemical Research in Chinese Universities*, Vol. 25, no. 6, pp. 966–970, 2009.

75. Adarsh, N., R. R. Avirah, and D. Ramaiah, "Tuning photosensitized singlet oxygen generation efficiency of novel aza-BODIPY dyes," *Organic Letters*, Vol. 13, no. 8, p. 2146, 2010.

76. Jaque, D., L. M. Maestro, B. Del Rosal, P. Haro-Gonzalez, A. Benayas, J. L. Plaza, E. M. Rodriguez, and J. G. Sole, "Nanoparticles for photothermal therapies," *Nanoscale*, Vol. 6, no. 16, pp. 9494–9530, 2014.

77. Aoshiba, K., N. Yokohori, and A. Nagai, "Alveolar wall apoptosis causes lung destruction and emphysematous changes," *American Journal of Respiratory Cell and Molecular Biology*, Vol. 28, no. 5, pp. 555–562, 2003.

78. Yin, Y., W. C. DeWolf, and A. Morgentaler, "Experimental Cryptorchidism Induces Testicular Germ Cell Apoptosis by p53-Dependent and -Independent Pathways In Mice," *Biology of Reproduction*, Vol. 58, no. 2, pp. 492–496, 1998.

79. Moesta, K. T., A. Dmytrijuk, P. Schlag, and T. S. Mang, "Individual in vitro sensitivities of human pancreatic carcinoma cell lines to photodynamic therapy," *SPIE*, Vol. 1645, pp. 43–51, 1992.

80. Gómez, S., M. Del Mont Llosas, J. Verdú, S. Roura, J. Lloreta, M. Fabre, and A. García De Herreros, "Independent regulation of adherens and tight junctions by tyrosine phosphorylation in Caco-2 cells," *Biochimica et Biophysica Acta - Molecular Cell Research*, Vol. 1452, no. 2, pp. 121–132, 1999.

81. Gkonos, P. J., F. Guo, and K. L. Burnstein, "Type 1 Vasoactive Intestinal Peptide Receptor Expression in PC3 / AR Cells Is Evidence of Prostate Epithelial Differentiation," *The Prostate*, Vol. 42, no. August 1999, pp. 137–144, 2000.

82. Komar-Stossel, C., E. Gross, E. Dery, N. Corchia, K. Meir, I. Fried, and R. Abramovitch, "TL-118 and gemcitabine drug combination display therapeutic efficacy in a mycn amplified orthotopic neuroblastoma murine model - Evaluation by MRI," *PLoS ONE*, Vol. 9, no. 3, pp. 1–8, 2014.

83. Böhmer, R. M., and G. Morstyn, "Uptake of hematoporphyrin derivative by normal and malignant cells: effect of serum, pH, temperature, and cell size," *Cancer Research*, Vol. 45, no. 11 Pt 1, pp. 5328–34, 1985.

84. Aveline, B., T. Hasan, and R. W. Redmond, "Photophysical and Photosensitizing Properties of Benzoporphyrin Derivative Monoacid Ring a (Bpd-Ma)," *Photochemistry and Photobiology*, Vol. 59, no. 3, pp. 328–335, 1994.

85. Cincotta, L., D. Szeto, E. Lampros, T. Hasan, and A. H. Cincotta, "Benzophenothiazine and benzoporphyrin derivative combination phototherapy effectively eradicates large murine sarcomas," *Photochemistry and Photobiology*, Vol. 63, no. 2, pp. 229–237, 1996.

86. Huang, H. C., S. Mallidi, J. Liu, C.-T. Chiang, Z. Mai, R. Goldschmidt, N. Ebrahim-Zahed, I. Rizvi, and Hasa, "Photodynamic therapy synergizes with irinotecan to overcome compensatory mechanisms and improve treatment outcomes in pancreatic cancer," *Cancer Research*, Vol. 76, no. 5, pp. 1066–1077, 2016.

87. Reiners, J. J., P. Agostinis, K. Berg, N. L. Oleinick, and D. Kessel, "Assessing autophagy in the context of photodynamic therapy John," *Autophagy*, Vol. 6, no. 1, pp. 7–18, 2010.

88. Rizvi, I., G. Obaid, S. Bano, T. Hasan, and D. Kessel, "Photodynamic therapy: Promoting in vitro efficacy of photodynamic therapy by liposomal formulations of a photosensitizing agent," *Lasers in Surgery and Medicine*, Vol. 50, no. 5, pp. 499–505, 2018.

89. Kessel, D., and J. J. Reiners, "Enhanced Efficacy of Photodynamic Therapy via a Sequential Targeting Protocol," *Photochemistry and Photobiology*, Vol. 90, no. 4, pp. 889–895, 2014.

90. Kessel, D., "Photodynamic therapy: Promotion of efficacy by a sequential protocol," *Journal of Porphyrins and Phthalocyanines*, Vol. 20, no. 1-4, pp. 302–306, 2016.

91. Kessel, D., "Subcellular Targeting as a Determinant of the Efficacy of Photodynamic Therapy," *Photochemistry and Photobiology*, Vol. 93, no. 2, pp. 609–612, 2017.

92. Celli, J. P., I. Rizvi, C. L. Evans, A. O. Abu-Yousif, and T. Hasan, "Quantitative imaging reveals heterogeneous growth dynamics and treatment-dependent residual tumor distributions in a three-dimensional ovarian cancer model," *Journal of Biomedical Optics*, Vol. 15, no. 5, p. 051603, 2010.

93. Kessel, D., "Apoptosis and associated phenomena as a determinants of the efficacy of photodynamic therapy," *Photochemical and Photobiological Sciences*, Vol. 14, no. 8, pp. 1397–1402, 2015.

94. Oleinick, N. L., R. L. Morris, and I. Belichenko, "The role of apoptosis in response to photodynamic therapy: What, where, why, and how," *Photochemical and Photobiological Sciences*, Vol. 1, no. 1, pp. 1–21, 2002.

95. Acedo, P., J. C. Stockert, M. Cañete, and A. Villanueva, "Two combined photosensitizers: A goal for more effective photodynamic therapy of cancer," *Cell Death and Disease*, Vol. 5, no. 3, pp. 1–12, 2014.

96. Schneider-Yin, X., A. Kurmanaviciene, M. Roth, M. Roos, A. Fedier, E. I. Minder, and H. Walt, "Hypericin and 5-aminolevulinic acid-induced protoporphyrin IX induce enhanced phototoxicity in human endometrial cancer cells with non-coherent white light," *Photodiagnosis and Photodynamic Therapy*, Vol. 6, no. 1, pp. 12–18, 2009.

97. Villanueva, A., J. C. Stockert, M. Cañete, and P. Acedo, "A new protocol in photodynamic therapy: Enhanced tumour cell death by combining two different photosensitizers," *Photochemical and Photobiological Sciences*, Vol. 9, no. 3, pp. 295–297, 2010.

98. Gyenge, E. B., D. Lüscher, P. Forny, M. Antoniol, G. Geisberger, H. Walt, G. Patzke, and C. Maake, "Photodynamic Mechanisms induced by a Combination of Hypericin and a Chlorin Based-Photosensitizer in Head and Neck Squamous Cell Carcinoma Cells," *Photochemistry and Photobiology*, Vol. 89, no. 1, pp. 150–162, 2013.

99. Granville, D. J., J. G. Levy, and D. W. Hunt, "Photodynamic Treatment with Benzoporphyrin Derivative Monoacid Ring a Produces Protein Tyrosine Phosphorylation Events and DNA Fragmentation in Murine P815 Cells," *Photochemistry and Photobiology*, Vol. 67, no. 3, pp. 358–362, 1998.

100. Lam, M., N. L. Oleinick, and A. L. Nieminen, "Photodynamic therapy-induced apoptosis in epidermoid carcinoma cells: Reactive oxygen species and mitochondrial inner membrane permeabilization," *Journal of Biological Chemistry*, Vol. 276, no. 50, pp. 47379–47386, 2001.

101. Oleinick, N. L., and H. H. Evans, "The photobiology of photodynamic therapy: cellular targets and mechanisms," *Radiation Research*, Vol. 150, no. 5s, pp. S146—-S156, 1998.

102. Yousefi, S., R. Perozzo, I. Schmid, A. Ziemiecki, T. Schaffner, L. Scapozza, T. Brunner, and H. U. Simon, "Calpain-mediated cleavage of Atg5 switches autophagy to apoptosis," *Nature Cell Biology*, Vol. 8, no. 10, pp. 1124–1132, 2006.

103. Kessel, D., and J. J. Reiners, "Effects of Combined Lysosomal and Mitochondrial Photodamage in a Non Small-Cell Lung Cancer Cell Line: the Role of Paraptosis," *Photochemistry and Photobiology*, Vol. 93, no. 6, pp. 1502–1508, 2017.

104. Foster, T. H., R. S. Murant, R. G. Bryant, R. S. Knox, S. Gibson, and R. Hilf, "Oxygen Consumption and Diffusion Effects in Photodynamic Therapy," *Radiation Research*, Vol. 126, no. 3, pp. 296–303, 1991.

105. Foster, T. H., D. F. Hartley, M. G. Nichols, and R. Hilf, "Fluence Rate Effects in Photodynamic Therapy of Multicell Tumor Spheroids," *Cancer Research*, Vol. 53, no. 6, pp. 1249–1254, 1993.

106. Nichols, M. G., and T. H. Foster, "Oxygen diffusion and reaction kinetics in the photodynamic therapy of multicell tumour spheroids," *Physics in Medicine and Biology*, Vol. 39, no. 12, pp. 2161–2181, 1994.

107. Rizvi, I., A.-l. Bulin, and E. Briars, *Mind the Gap : 3D Models in Photodynamic Therapy*, The Royal Society of Chemistry, 2016.

108. Benam, K. H., S. Dauth, B. Hassell, A. Herland, A. Jain, K.-J. Jang, K. Karalis, H. J. Kim, L. MacQueen, R. Mahmoodian, S. Musah, Y.-s. Torisawa, A. D. van der Meer, R. Villenave, M. Yadid, K. K. Parker, and D. E. Ingber, "Engineered In Vitro Disease Models," *Annual Review of Pathology: Mechanisms of Disease*, Vol. 10, no. 1, pp. 195–262, 2015.

109. Malandrino, A., R. D. Kamm, and E. Moeendarbary, "In Vitro Modeling of Mechanics in Cancer Metastasis," *ACS Biomaterials Science and Engineering*, Vol. 4, no. 2, pp. 294–301, 2018.

110. Polacheck, W. J., R. Li, S. G. M. Uzel, and R. D. Kamm, "Microfluidic platforms for mechanobiology William," *Lab Chip*, Vol. 13, no. 12, pp. 2252–2267, 2013.

111. Demou, Z. N., "Gene expression profiles in 3D tumor analogs indicate compressive strain differentially enhances metastatic potential," *Annals of Biomedical Engineering*, Vol. 38, no. 11, pp. 3509–3520, 2010.

112. Tse, J. M., G. Cheng, J. A. Tyrrell, S. A. Wilcox-Adelman, Y. Boucher, R. K. Jain, and L. L. Munn, "Mechanical compression drives cancer cells toward invasive phenotype," *Proceedings of the National Academy of Sciences*, Vol. 109, no. 3, pp. 911–916, 2012.

113. Avvisato, C. L., X. Yang, S. Shah, B. Hoxter, W. Li, R. Gaynor, R. Pestell, A. Tozeren, and S. W. Byers, "Mechanical force modulates global gene expression and beta-catenin signaling in colon cancer cells," *Journal of Cell Science*, Vol. 120, no. 15, pp. 2672–2682, 2007.

114. Butcher, D. T., T. Alliston, and V. M. Weaver, "A tense situation: forcing tumour progression," *Nature Reviews Cancer*, Vol. 9, no. 2, pp. 108–122, 2009.

115. Jain, R. K., J. D. Martin, and T. Stylianopoulos, "The role of mechanical forces in tumor growth and therapy," *Annual Review of Biomedical Engineering*, Vol. 16, pp. 321–346, 2014.

116. Stylianopoulos, T., J. D. Martin, V. P. Chauhan, S. R. Jain, B. Diop-Frimpong, N. Bardeesy, B. L. Smith, C. R. Ferrone, F. J. Hornicek, Y. Boucher, L. L. Munn, and R. K. Jain, "Causes, consequences, and remedies for growth-induced solid stress in murine and human tumors," *Proceedings of the National Academy of Sciences*, Vol. 109, no. 38, pp. 15101–15108, 2012.

117. Yu, H., J. K. Mouw, and V. M. Weaver, "Forcing Form and Function: Biomechanical Regulation of Tumor Evolution," *Trends in Cell Biology*, Vol. 21, no. 1, pp. 47–56, 2011.

118. Cheng, G., J. Tse, R. K. Jain, and L. L. Munn, "Micro-environmental mechanical stress controls tumor spheroid size and morphology by suppressing proliferation and inducing apoptosis in cancer cells," *PLoS ONE*, Vol. 4, no. 2, 2009.

119. Roose, T., P. A. Netti, L. L. Munn, Y. Boucher, and R. K. Jain, "Solid stress generated by spheroid growth estimated using a linear poroelasticity model," *Microvascular Research*, Vol. 66, no. 3, pp. 204–212, 2003.

120. Sarntinoranont, M., F. Rooney, and M. Ferrari, "Interstitial stress and fluid pressure within a growing tumor," *Annals of Biomedical Engineering*, Vol. 31, no. 3, pp. 327–335, 2003.

121. Paszek, M. J., N. Zahir, K. R. Johnson, J. N. Lakins, G. I. Rozenberg, A. Gefen, C. A. Reinhart-King, S. S. Margulies, M. Dembo, D. Boettiger, D. A. Hammer, and V. M. Weaver, "Tensional homeostasis and the malignant phenotype," *Cancer Cell*, Vol. 8, no. 3, pp. 241–254, 2005.

122. Chin, L., Y. Xia, D. E. Discher, and P. A. Janmey, "Mechanotransduction in cancer," *Current Opinion in Chemical Engineering*, Vol. 11, pp. 77–84, 2016.

123. Wang, N., J. P. Butler, and D. E. Ingber, "Mechanotransduction Across the Cell Surface and Through the Cytoskeleton," *Science*, Vol. 260, no. May, pp. 1124–1128, 1993.

124. Wozniak, M. A., K. Modzelewska, L. Kwong, and P. J. Keely, "Focal adhesion regulation of cell behavior," *Biochimica et Biophysica Acta - Molecular Cell Research*, Vol. 1692, no. 2-3, pp. 103–119, 2004.

125. Levental, K. R., H. Yu, L. Kass, J. N. Lakins, M. Egeblad, J. T. Erler, S. F. Fong, K. Csiszar, A. Giaccia, W. Weninger, M. Yamauchi, D. L. Gasser, and V. M. Weaver, "Matrix Crosslinking Forces Tumor Progression by Enhancing Integrin Signaling," *Cell*, Vol. 139, no. 5, pp. 891–906, 2009.

126. Ulrich, T. A., E. M. de Juan Pardo, and S. Kumar, "The mechanical rigidity of the extracellular matrix regulates the structure, motility, and proliferation of glioma cells," *Cancer Research*, Vol. 69, no. 10, pp. 4167–4174, 2009.

127. Lang, N. R., K. Skodzek, S. Hurst, A. Mainka, J. Steinwachs, J. Schneider, E. Aifantis, and B. Fabry, "Biphasic response of cell invasion to matrix stiffness in 3-dimensional biopolymer networks," *Acta Biomaterialia*, Vol. 13, no. 61-67, pp. 1–14, 2016.

128. Pathak, A., and S. Kumar, "Independent regulation of tumor cell migration by matrix stiffness and confinement," *Proceedings of the National Academy of Sciences*, Vol. 109, no. 26, pp. 10334–10339, 2012.

129. Cassereau, L., Y. A. Miroshnikova, G. Ou, J. Lakins, and V. M. Weaver, "A 3D tension bioreactor platform to study the interplay between ECM stiffness and tumor phenotype," *Journal of Biotechnology*, Vol. 193, pp. 66–69, 2015.

130. Rubashkin, M. G., L. Cassereau, R. Bainer, C. C. Dufort, Y. Yui, G. Ou, M. J. Paszek, M. W. Davidson, Y. Y. Chen, and V. M. Weaver, "Force engages vinculin and promotes tumor progression by enhancing PI3-kinase activation of phosphatidylinositol (3,4,5)-triphosphate," *Cancer Research*, Vol. 74, no. 17, pp. 4597–4611, 2014.

131. Nia, H. T., M. Datta, G. Seano, P. Huang, L. L. Munn, and R. K. Jain, "Quantifying solid stress and elastic energy from excised or in situ tumors," *Nature Protocols*, Vol. 13, no. 5, pp. 1091–1105, 2018.

132. Wilson, W. R., and M. P. Hay, "Targeting hypoxia in cancer therapy," *Nature Reviews Cancer*, Vol. 11, no. 6, pp. 393–410, 2011.

133. Helmlinger, G., P. A. Netti, H. C. Lichtenbeld, R. J. Melder, and R. K. Jain, "Solid stress inhibits the growth of multicellular tumor spheroids," *Nature Biotechnology*, Vol. 15, no. 8, pp. 778–783, 1997.

134. Patra, B., C.-C. Peng, W.-H. Liao, C.-H. Lee, and Y.-C. Tung, "Drug testing and flow cytometry analysis on a large number of uniform sized tumor spheroids using a microfluidic device," *Scientific Reports*, Vol. 6, no. 1, p. 21061, 2016.

135. Gjorevski, N., A. S. Piotrowski, V. D. Varner, and C. M. Nelson, "Dynamic tensile forces drive collective cell migration through three-dimensional extracellular matrices," *Scientific Reports*, Vol. 5, no. May, p. 11458, 2015.

136. Hyler, A. R., N. C. Baudoin, M. S. Brown, M. A. Stremler, D. Cimini, R. V. Davalos, and E. M. Schmelz, "Fluid shear stress impacts ovarian cancer cell viability, subcellular organization, and promotes genomic instability," *PLoS ONE*, Vol. 13, no. 3, pp. 1–21, 2018.

137. Das, T., T. K. Maiti, and S. Chakraborty, "Augmented stress-responsive characteristics of cell lines in narrow confinements," *Integrative Biology*, Vol. 3, no. 6, pp. 684–695, 2011.

138. Haessler, U., J. C. Teo, D. Foretay, P. Renaud, and M. A. Swartz, "Migration dynamics of breast cancer cells in a tunable 3D interstitial flow chamber," *Integrative Biology*, Vol. 4, no. 4, pp. 401–409, 2012.

139. Mak, M., C. A. Reinhart-King, and D. Erickson, "Elucidating mechanical transition effects of invading cancer cells with a subnucleus-scaled microfluidic serial dimensional modulation device," *Lab on a Chip*, Vol. 13, no. 3, pp. 340–348, 2013.

140. Riching, K. M., B. L. Cox, M. R. Salick, C. Pehlke, A. S. Riching, S. M. Ponik, B. R. Bass, W. C. Crone, Y. Jiang, A. M. Weaver, K. W. Eliceiri, and P. J. Keely, "3D collagen alignment limits protrusions to enhance breast cancer cell persistence," *Biophysical Journal*, Vol. 107, no. 11, pp. 2546–2558, 2015.

141. Ma, P., X. Shen, P. Tan, L. Yang, and W. Liu, "Effect of matrix rigidity on organ-specific capture of tumor cells by flow," *Cellular and Molecular Biology*, Vol. 63, no. 4, pp. 10–15, 2017.

142. Lengyel, E., "Ovarian cancer development and metastasis," *American Journal of Pathology*, Vol. 177, no. 3, pp. 1053–1064, 2010.

143. Spring, B. Q., A. O. Abu-Yousif, A. Palanisami, I. Rizvi, X. Zheng, Z. Mai, S. Anbil, R. B. Sears, L. B. Mensah, R. Goldschmidt, S. S. Erdem, E. Oliva, and T. Hasan, "Selective treatment and monitoring of disseminated cancer micrometastases in vivo using dual-function, activatable immunoconjugates," *Proceedings of the National Academy of Sciences*, pp. E933–E942, 2014.

144. Ip, C. K., S. S. Li, M. Y. Tang, S. K. Sy, Y. Ren, H. C. Shum, and A. S. Wong, "Stemness and chemoresistance in epithelial ovarian carcinoma cells under shear stress," *Scientific Reports*, Vol. 6, pp. 1–11, 2016.

145. Kwiatkowski, S., B. Knap, D. Przystupski, J. Saczko, E. Kędzierska, K. Knap-Czop, J. Kotlińska, O. Michel, K. Kotowski, and J. Kulbacka, "Photodynamic therapy - mechanisms, photosensitizers and combinations," *Biomedicine and Pharmacotherapy*, Vol. 106, no. June, pp. 1098–1107, 2018.